Available online at www.sciencedirect.com
SCIENCE DIRECT®
Coordination Chemistry Reviews 249 (2005) 97–129
COORDINATION CHEMISTRY REVIEWS
www.elsevier.com/locate/ccr

Review

Ligand K-edge X-ray absorption spectroscopy: covalency of ligand–metal bonds☆

Edward I. Solomon[a,*], Britt Hedman[b,1], Keith O. Hodgson[a,b], Abhishek Dey[a], Robert K. Szilagyi[c]

[a] *Department of Chemistry, Stanford University, Stanford, CA 94305, USA*
[b] *Stanford Synchrotron Radiation Laboratory, Stanford, CA 94309, USA*
[c] *Department of Chemistry and Biochemistry, Montana State University, MT 59717, USA*

Received 1 October 2003; accepted 12 March 2004
Available online 23 July 2004

Contents

☆ For Thematic Issue of Coordination Chemistry Review entitled Synchrotron Radiation in Inorganic and Bioinorganic Chemistry.

* Corresponding author. Tel.: +1-650-723-4694; fax: +1-650-703-0553.
E-mail addresses: edward.solomon@stanford.edu (E.I. Solomon), hedman@ssrl.slac.stanford.edu (B. Hedman).
[1] Co-corresponding author. Tel.: +1-650-926-3052; fax: +1-650-925-4100.

0010-8545/$ – see front matter
doi:10.1016/j.ccr.2004.03.020

Abstract

The ligand K-edge probes the ligand 1s → valence np transitions. These transitions acquire intensity when the ligand is bound to an open shell metal ion. This intensity quantifies the amount of ligand character in the metal d orbitals, hence the covalency of the ligand–metal bond. In this review the methodology is developed and applied to copper proteins, iron–sulfur sites and nickel dithiolene complexes, as examples. These illustrate the power and impact of this method in evaluating covalency contributions to electron transfer pathways, reduction potentials, H-bond interactions, electron delocalization in mixed-valent systems and small molecule reactivity.

Keywords: Ligand K-edge XAS; Cu_A; Blue copper; Iron–sulfur cluster; Nickel dithiolene; DFT

1. Introduction

Quantifying covalency, defined here as the coefficients of ligand character in the valence metal d derived molecular orbitals, has been the long term goal of physical–inorganic chemists. Covalency is responsible for many of the physical properties of transition metal systems and for reactivity. In inorganic materials, the covalency of the metal–ligand bond leads to the exchange coupling between metal ions responsible for their magnetic properties and to dispersion of the HOMO and LUMO into bands leading to conductivity. In inorganic and bioinorganic chemistry, the covalency of the metal–ligand bonds can lead to small molecule reactivity, enhance specific superexchange pathways for electron transfer, and activate metal sites for catalysis.

There are many traditional methods to experimentally quantify the covalency of the valence orbitals of transition metal complexes [1]. These usually involve ground state studies. In EPR spectroscopy, the quantitative deviation of the g values from 2.0023 derives from the combination of spin-orbit coupling with excited states and the covalent reduction of this coupling [2]. The g values, however, do not allow a direct experimental estimate of covalency as a number of different bonding interactions contribute to each g_i value; these are best used to evaluate electronic structure calculations [3]. Metal hyperfine coupling is another important experimental probe of covalency as delocalization of the electron spin density onto the ligands reduces its hyperfine coupling to the metal center [2]. However, there are three contributions to metal hyperfine, Fermi contact, spin dipolar, and orbital dipolar coupling, all of similar magnitude and different signs; each is affected differently by covalent delocalization onto the ligands. The most direct ground state probe of covalency is ligand superhyperfine coupling [4] which is often small and best measured by double resonance (electron nuclear double resonance, ENDOR) or pulsed (electron spin echo envelope modulation, ESEEM) EPR methods [5]. The amplitude and anisotropy of the ligand superhyperfine coupling directly probes the delocalization of the electron spin density into s and p orbitals of the ligand, thus quantifying covalency and hybridization. This, however, requires an EPR active site and only probes molecular orbitals containing unpaired electrons.

For bound excited states, charge transfer transition energies and intensities can be used within the context of a valence bond configuration interaction (VBCI) model to approximately estimate covalent delocalization over the ligands [6]. This has been particularly useful in bridged magnetic dimers where the charge transfer mixing into the ground state provides the superexchange pathway for magnetic coupling. Finally, in ionized final states, i.e. photoelectron spectroscopy (PES), the intensity dependence of the valence band peaks with input photon energy, and the intensity of shake up satellites in valence and core regions, analyzed in the context of a VBCI model, also quantify covalent mixing [7]. However, these are complicated by large final state effects associated with the change in electron repulsion on ionization (see PES reviews in this volume).

Given the complications and restrictions of existing experimental methods in estimating covalency, we have developed a new method based on X-ray absorption spectroscopy (XAS) at the ligand K-edge [8]. As described in other chapters in this volume, traditional XAS studies involve metal K-edges. These focus on the 1s → 3d transitions which are weak (quadrupole allowed) [9] and gain intensity due to low symmetry mixing of metal p character [10]. Thus metal K-edges probe an important mixing, but have low sensitivity to the amount of metal character in the valence orbitals. Metal L-edges are at much lower energy (for 3d transition metal complexes in the UHV 400–1000 eV region) and therefore can be studied at higher resolution (∼0.3 eV versus >1.2 eV for metal K-edges) [11]. As they involve the 2p → 3d transitions, the transition intensity directly reflects the amount of metal d character in a valence molecular or-

bital [12]. However, this intensity reflects the net effect of the entire ligand environment and does not probe specific ligand–metal bonds.

The ligand K-edge involves the ligand 1s → np transition. Since the 1s orbital is localized on the ligand and the s → p transition is electric dipole allowed, the intensity of this transition quantifies the amount of ligand p character in the valence molecular orbital. This probes all singly-occupied and unoccupied acceptor orbitals of the transition metal complex that have a ligand np contribution and therefore provides a direct probe of the covalency of the ligand–metal bond.

In this review we first describe the experimental details of ligand K-edge XAS (Section 2) and then develop the methodology (Section 3), first for the d^9 configuration containing one hole, then for general d^n metal complexes. We also consider how molecular orbital derived results of covalency compare with those of ligand K-edge XAS approaches. The following sections describe the application of this methodology to a range of important problems in bioinorganic and inorganic chemistry. Here we focus on sulfur and chlorine K-edges where the methodology has been developed. Similar approaches can be applied in principle to any ligand K-edge, however there can be complications based on energy region of the ligand edge, effective nuclear charge on the metal and in some cases (i.e. N and O) these can only be accessible for model complexes. In Section 4 we consider blue copper and Cu_A centers, which play key roles in biological electron transfer. These centers have sulfur-Cu bonds for which the covalency (determined by ligand K-edge XAS) activates specific protein pathways for long-range electron transfer [13]. In Section 5 we consider iron–sulfur proteins, which are also involved in electron transfer. These consist of centers containing one to four Fe atoms, and a combination of thiolate, μ_2 and μ_3 sulfide ligation, displaying interesting mixed-valence properties that affect magnetic interactions over the cluster sites, and protein effects on the sulfur-iron bonds, which tune these centers for electron transfer. Finally, in Section 6 we consider nickel dithiolene bonding. The dithiolene ligand is generally important in bioinorganic chemistry, particularly in the oxo-molybdenum transferase enzymes. Also the nickel dithiolene series has played an important historical role in inorganic chemistry. Its non-innocent nature has been the focus of a number of studies on electron delocalization over the dithiolene ligand, and has recently been used to define a new reactivity with olefins. Ligand K-edge XAS is clearly a powerful new method in the arsenal of the physical–inorganic chemist to experimentally define the covalency of the ligand–metal bond.

2. The experiment

All ligand K-edge data presented in this review were measured at the Stanford Synchrotron Radiation Laboratory under ring conditions of 3 GeV and 60–100 mA. The experiments were performed on the 54-pole wiggler beam line 6-2 operating in high field (10 kG) mode with a fully tuned Si(1 1 1) double crystal monochromator followed by a Ni-coated harmonic rejection mirror.

2.1. Experimental setup

Beam line 6-2 is optimized for low-energy studies, with all optical elements under a differentially-pumping maintained vacuum, and with a single, in-hutch 127 μm beryllium window separating the experiment from ring vacuum. This Be window is protected from oxidation by a ∼4 in. He gas path terminated with a 6.35 μm polypropylene window. The beam thereafter passes in a He gas atmosphere through aperturing slits, an ionization chamber for I_0 measurements, and a 6.35 μm polypropylene window into the sample compartment (Fig. 1).

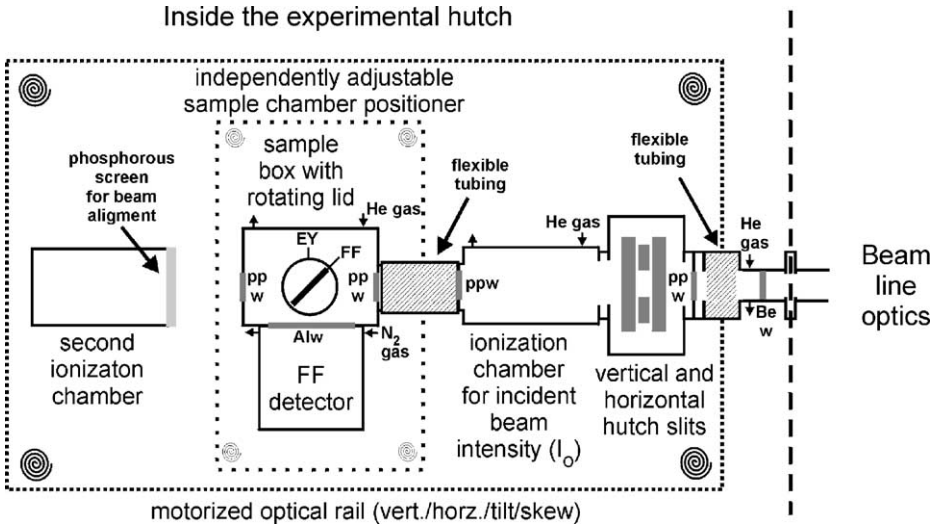

Fig. 1. Schematic representation of the experimental setup at SSRL BL6-2 (ppw: polypropylene window, Alw: aluminized Mylar window, Bew: beryllium window, EY: electron-yield, FF: fluorescence).

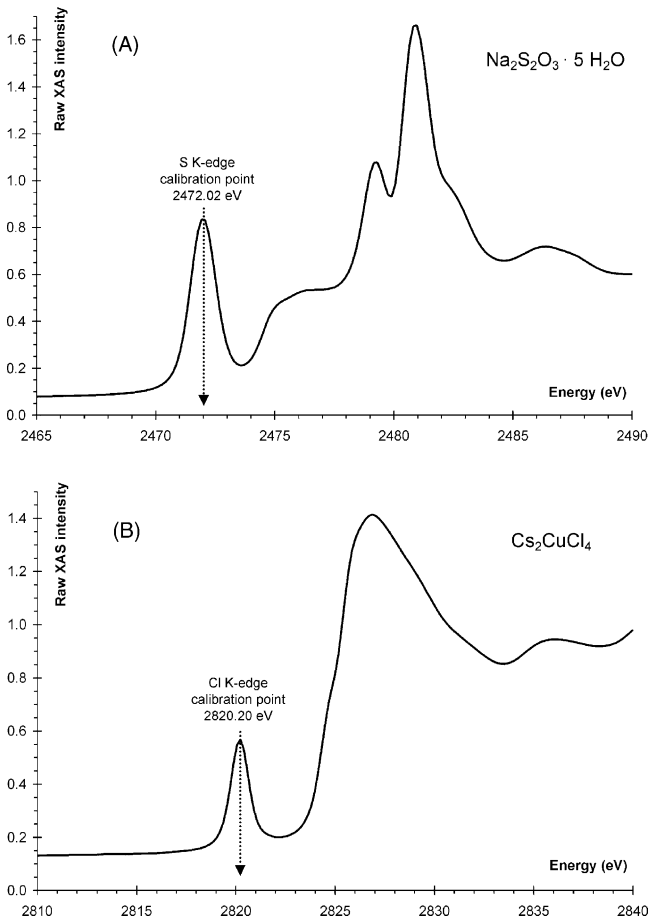

Fig. 2. Sodium thiosulfate (A) and cesium copper tetrachloride (B) calibration scans with marked calibration points.

The sample compartment is equipped with a rotating lid inset, which is set to 45° or 90° relative to the incident beam for fluorescence and electron-yield detection modes, respectively. For fluorescence excitation spectra measurements, a N_2-filled Lytle detector [14,15] is used without filter or Soller slits. For electron-yield measurements a detector is used, manufactured by The EXAFS Company [16]. This is equipped with a Ni grid for collecting Auger- and photoelectrons in a windowless setup between the grid and the sample. Due to the high absorption at low energies (2–4 keV), external energy calibration using a well-characterized standard is required. This is performed at regular intervals, often before and after each sample. For S and Cl K-edge experiments, the standards used are $Na_2S_2O_3{\cdot}5H_2O$ and Cs_2CuCl_4, and the sharp maximum of their first pre-edge feature is assigned at 2472.02 eV (Fig. 2A) and 2820.20 eV (Fig. 2B), respectively. The monochromator step size over the edge region is typically 0.08 eV, the energy resolution is ∼0.5 eV, and the reproducibility in energy determination is ∼0.1 eV, as determined from repeated calibration and sample measurements during separate experimental runs.

Solid samples are ground to an extremely fine powder, which is dusted thinly on Mylar tape (containing an acrylic adhesive determined to be free of sulfur and chlorine contaminants), and mounted across the window of an Al plate. The thin sample coverage on the tape is required to minimize the possibility of fluorescence self-absorption effects. For electron-yield experiments this is less of a concern, however, the tape needs to be conductively attached to the detector to eliminate any build up of charge on the sample surface, which can result in significant noise in the data. For air-sensitive compounds, all preparations are performed in a N_2-filled inert-atmosphere glovebox. In fluorescence detection, the front of the sample is sealed with an absorber-free 6.35 μm polypropylene window and the sample holder is exposed to air for less than 5 s, while being transferred from a sealed jar into the He atmosphere of the sample compartment at the beam line. Since the electron-yield experiments use a windowless setup the sample is mounted onto the back panel of the detector in the glovebox.

Protein samples are pre-equilibrated for ∼0.5–1 h with a de-ionized water-saturated He gas in a cold room at +4 °C, this minimizes bubble formation in the sample cell of He gas penetrating the thin sample compartment window. Thereafter an aliquot of ∼160 μL is transferred into a Pt-coated Al block sample cell, sealed with a polypropylene window on the front and with septum-sealed loading and gas-release holes on the top. For solutions, including dilute biological samples, the sample cell block is cooled by passing N_2 gas, which has passed through copper coils immersed in liquid N_2, through channels in the Al block body. The sample temperature is typically maintained at ∼+4 °C, measured at the sample block with a thermocouple. Solution samples with a lower melting point (organic solvents or biological samples with a glassing agent) are cooled down to ∼(−50) °C using a shroud around the sample cell, which is continuously purged with pre-cooled He gas.

The fluorescence detection technique has an ∼50–200 Å penetration depth [17] into the sample and provides good data for solids distributed thinly enough or dilute solutions in the range of 1–10 mM concentration. Although, electron-yield detection (collecting electrons emitted upon excited-state relaxation) with a sufficiently large collector voltage (∼200 V for the S and ∼300 V for the Cl K-edge, respectively) can also give reasonable data without the risk of self-absorption. However this detection technique is highly surface sensitive due to its limited penetration depth (at most 50 Å [18]).

2.2. Data reduction

The raw data are inspected graphically at the beam line to eliminate scans with beam, beam line or sample induced abnormalities. In particular, effects due to sample photoreduction, if present, are monitored and a determination is made as to whether enough scans are available to produce a reliable scan average at the initial oxidation state. If not, and if a suitable oxidant is available, the sample is recovered, re-oxidized, and re-measured. Provided that the first scan of

the re-oxidized sample superimposes on the previous unaffected scans, the experiment is continued until the desired signal-to-noise has been obtained. Depending on the behavior of the sample in the beam, the extrapolated curve, obtained by a logarithmic projection of the critical data points at certain energy positions (such as an edge transition maximum) to zero time, can be used in further analysis.

Pre- and post-data calibration scans (see Fig. 2) are compared and the energy scale of the data is adjusted accordingly. The acceptable data scans are then averaged, and a smooth second-order polynomial background is fit to the pre-edge region and subtracted from the entire spectrum (Fig. 3A). Normalization of the data is accomplished by fitting a flattened second-order polynomial or straight line to the post-edge region and normalizing to an edge jump of 1.0 at 2490 and 2840 eV for the S and Cl K-edges, respectively (Fig. 3B). In protein samples with free Cys or Met residues or samples with absorbers not contributing to the pre-edge

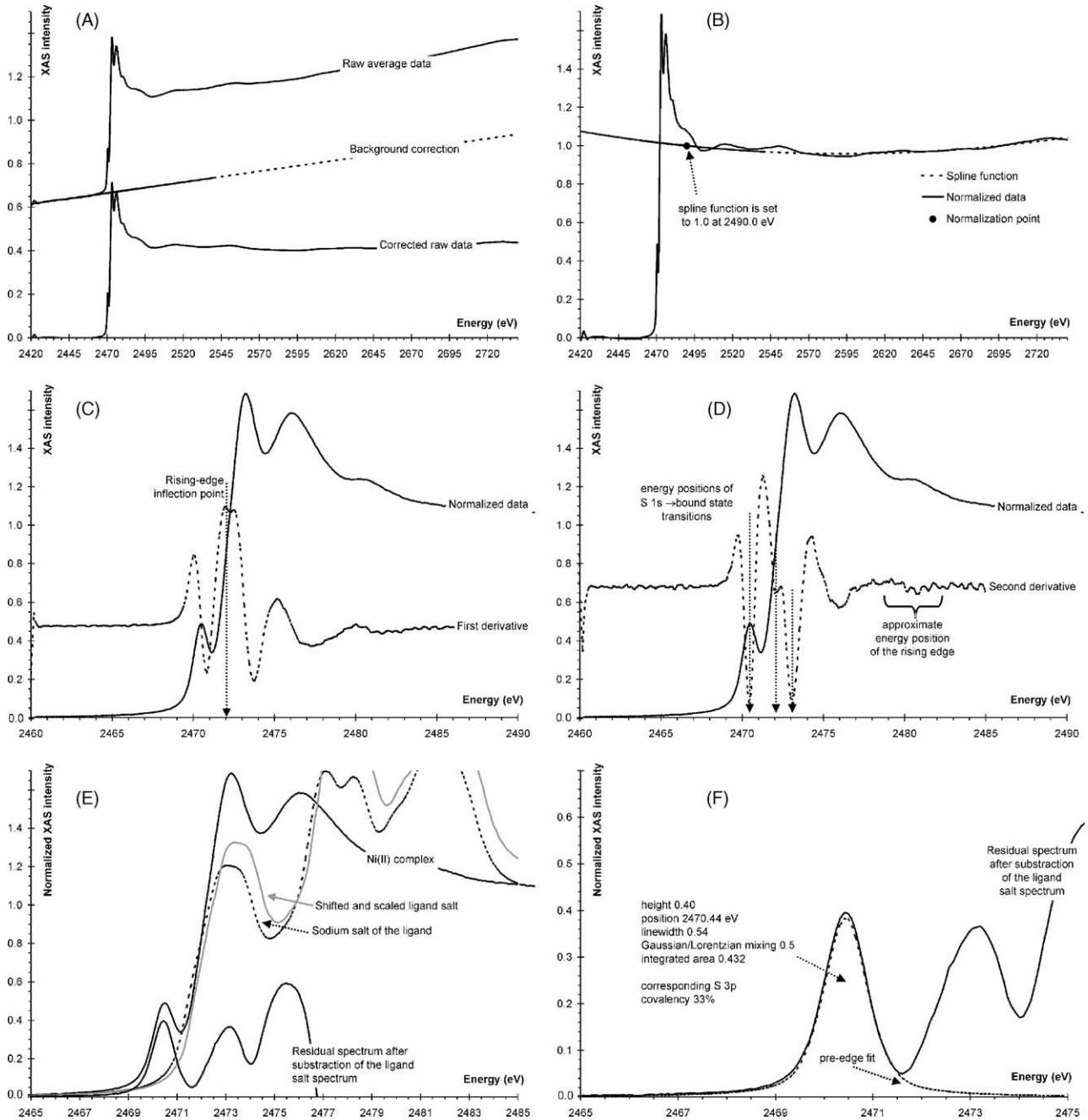

Fig. 3. Data reduction steps of the calibrated and averaged S K-edge spectrum of $(Et_4N)_2[Ni(S\text{-}2Ph\text{-}C_6H_4)_4]$ complex [K.R. Williams, B. Hedman, K.O. Hodgson, E.I. Solomon Inorg. Chim. Acta 263 (1997) 315]. (A) Raw data with pre-edge background correction. (B) Spline function and normalization. (C) Smoothed first derivative of the normalized data in the rising-edge energy region. (D) Smoothed second derivative of the normalized data in the rising-edge energy region. (E) Subtraction of the ligand salt spectrum. (F) Fitting of the pre-edge feature.

feature, the spectrum needs to be renormalized by the ratio of the total and the contributing absorbers for the covalency determinations described in this review. Obviously buffers, reactants or any contamination containing the absorber atom must be exchanged or removed before data collection. Otherwise the normalization and thus the quantitation of spectral features cannot be carried out.

Energy positions of features in the normalized spectrum are generally obtained from the minima in the second derivative of the data (Fig. 3D). The rising edge positions for similar ligands are determined from the energies of the maxima of the first derivative (i.e. inflection points) in the rising-edge region (Fig. 3C). Comparison of rising-edge positions in different ligands can be obscured by high energy bound state transitions, such as absorber 1s to σ or π-type antibonding ligand-based molecular orbitals or by the splitting to overlapping orbitals giving rise of various spectral features.

If the spectrum of the uncoordinated ligand or ligand salt is available and the nature of the unoccupied ligand orbitals is not significantly perturbed in the complex, the spectrum of the free ligand can be used to subtract the rising-edge jump and related features from the data giving a clean plot of the pre-edge region (Fig. 3E). The pre-edge features are fitted by pseudo-Voigt lines with a fixed 1:1 ratio of Lorentzian to Gaussian contributions using the program EDG_FIT [19], which utilizes the double precision version of the MINPAK fitting library [20]. The use of pseudo-Voigt line shape is justified, since the pre-edge features are expected to be a convolution of the Lorentzian transition envelope [21] and the Gaussian line shape imposed by the beam line optics [14,22,23]. The fitting ranges are typically 2465–2475 eV (Fig. 3F) and 2818–2826 eV for S and Cl K pre-edges, respectively. The linewidths are generally found to be about 0.5–0.6 eV for S based pre-edge features and about 0.1 eV wider for Cl. In all fits, the minimum number of required functions is utilized. The final intensity values, calculated as the product of peak heights and linewidths, are based on the average of several good fits. In addition to the error resulting from the background correction and fitting procedure (ca. 2%), normalization procedures can introduce ca. 3% error in the total pre-edge peak areas.

3. Methodology

3.1. Theoretical background

The ligand K-edge XAS of a chloride bound to Cu^{2+} in square planar $[Cu(II)Cl_4]^{2-}$ (d^9) shows a well defined pre-edge feature which is not present in the corresponding $[Zn(II)Cl_4]^{2-}$ (d^{10}) spectrum (Fig. 4) [8a]. This feature, at 2820 eV, must then be related to the singly occupied molecular orbital (SOMO) of the Cu(II) complex.

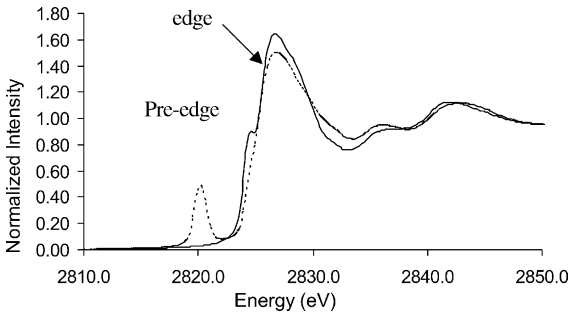

Fig. 4. Chlorine K-edge XAS spectra of $[CuCl_4]^{2-}$ (dotted) and $[ZnCl_4]^{2-}$ (solid) showing the distinct pre-edge feature of $[CuCl_4]^{2-}$.

The SOMO of $[Cu(II)Cl_4]^{2-}$ is expressed as the antibonding combination of metal orbitals |M> with ligand valence orbitals |L⟩ as in Eq. (1)

$$\Psi_{SOMO} = \sqrt{(1-\alpha^2)}|M> -\alpha|L\rangle \quad (1)$$

This gives α^2 as the total ligand character (covalency) in the SOMO. The ligand part of Eq. (1) can be expressed as

$$|L>= \sum_q \sum_j C_{q,j\mathrm{SOMO}}|L_{q,j}\rangle \quad (2)$$

where q sums over all ligands and j sums over individual ligand valence orbitals (s, p and d) contributing to the wavefunction and $C_{q,j\mathrm{SOMO}}$ are the coefficients of the contributing valence orbitals to the symmetry-adapted linear combinations (SALC). In the case of ligands such as chloride, thiolate, and sulfide, the contributions of 3s and 3d orbitals are far less significant (limited to a few percent) than the 3p contribution. This is primarily due to the larger energy separations of 3s and 3p orbitals and reduced hybridization of third row ligand atoms compared to second row ligand atoms.

The donor MO ψ_k is a linear combination of ligand 1s orbitals

$$|\Psi_k\rangle = \sum_r b_{r,k}|1s_{r+}\rangle \quad (3)$$

where b is the coefficient of the 1s contribution from the different ligands and r sums over all ligands.

The intensity of the transition from the ligand 1s to the SOMO is given by the following expression using the dipole length approximation and Fermi's golden rule [24,25]

$$I \propto |\langle F_k|\sum_A Z_A\vec{R}_A - \sum_i \vec{r}_i|I\rangle|^2 \approx |\langle\Psi_{\mathrm{SOMO}}|\boldsymbol{r}|\Psi_k\rangle|^2 \quad (4)$$

where A sums over all the nuclei (at R_A) and i sums over all the electrons (at $\boldsymbol{r}_i$). F_K is the many electron final state and I is the initial state. Using the expressions obtained for $|\Psi_k\rangle$ and $|\Psi_{\mathrm{SOMO}}\rangle$ from Eqs. (1)–(3), respectively, the intensity expression in 4 becomes:

$$I\alpha\left(\sqrt{(1-\alpha)^2}\sum_r b_{r,k}\langle M|\boldsymbol{r}|1s_r\rangle - \alpha\sum_r\sum_j\sum_q C_{q,j\mathrm{SOMO}}b_{rk}\langle L_{q,j}|\boldsymbol{r}|1s_r\rangle\right)^2 \quad (5)$$

The first integral, an overlap integral between metal centered and ligand centered orbitals, is very small (on the order of 10^{-4}) [26] and hence can be neglected with respect to the second integral, which is a two-centered electric dipole integral. The overlap integrals between orbitals on different ligands ($q \neq r$) in the second integral are neglected, as they will have negligible contribution compared to transition moment integrals between orbitals on same atom ($q = r$). On applying the electric-dipole selection rule (i.e. $j = p$ orbital allowed, giving strong transitions, while $j = s$ is forbidden and $j = d$ is quadrupole allowed, giving weak transitions) the second integral becomes

$$|\langle L_{q,p}|\boldsymbol{r}|1s_q\rangle| = \sqrt{\frac{(1-k_{\mathrm{SOMO}})^2}{3}}\langle \boldsymbol{r}\rangle_{np_q 1s_q}\vec{e}_{p_q} \tag{6}$$

where $\langle \boldsymbol{r}\rangle_{np_q 1s_q} = \langle \mathrm{Rad}_{np_q}|\boldsymbol{r}|\mathrm{Rad}_{1s_q}\rangle$ (where Rad is the radial part of the wavefunction), $\vec{e}_{p_q}$ is the unit vector along the ligand p-orbital axis which contributes to the SOMO, and k_{SOMO} is the relative contribution of the ψ_{ns} orbital to the total ligand valence hybrid orbital contributing to the SOMO wavefunction. Hence $(1-k_{\mathrm{SOMO}})^2$ is the ligand ψ_{np} character in the SOMO. Using Eq. (6), the final expression for the matrix elements for transition dipole operator in Eq. (4) becomes

$$|\langle \Psi_{\mathrm{SOMO}}|\boldsymbol{r}|\Psi_k\rangle| = -\alpha\sum_q C_{q,p\mathrm{SOMO}} b_k \sqrt{\frac{(1-k_{\mathrm{SOMO}})^2}{3}}\langle \boldsymbol{r}\rangle_{np_q 1s_q}\vec{e}_{p_q} \tag{7}$$

where the C's are the coefficients of the SALC's of the ligand np orbitals in the ligand part of the SOMO. The simplest case is when there is one ligand atom of specific chemical interest (i.e. $C^2_{q,p} = 1$) contributing to the SOMO. The expression for the intensity in Eq. (7) then becomes

$$I\alpha|\langle \Psi_{\mathrm{SOMO}}|\boldsymbol{r}|\Psi_k\rangle|^2 = -\tfrac{1}{3}\alpha^2(1-k_{\mathrm{SOMO}})^2\langle \boldsymbol{r}\rangle^2_{\mathrm{np},1s} \tag{8}$$

Eq. (8) has a straight forward physical significance. The intensity of the 1s → SOMO transition increases as α^2, the total ligand character in the SOMO and as the p character of this ligand contribution to the SOMO increases $(1-k_{\mathrm{SOMO}})^2$. In absolute terms, for a particular ligand atom, the factor $1/3\langle \boldsymbol{r}\rangle^2_{\mathrm{np}_q 1s_q}$ is the intrinsic intensity of an 1s → np transition.

The intensity of the pre-edge transition depends on the radial functions of the ligand 1s and 3p orbitals (the overlap integral $\langle \boldsymbol{r}\rangle_{\mathrm{np}_q 1s_q}$ in Eq. (8)). Hartree–Fock calculations were performed on free Cl and S atoms [26] to evaluate the effect of a change of the charge of a ligand on the transition integral. The overlap integral decreases with increase in negative charge on the contributing atom on the ligand. This is because the 3p orbitals expand more than the 1s, as Z_{eff} of the ligand decreases, decreasing the overlap between these orbitals. However, the charge dependence of this integral, when translated into percentage ligand character, is linear and very small. An increase in the effective Cl 3p population from 5.22 to 5.69 only causes the value of the integral to change by some 3%. The changes for sulfur are somewhat more pronounced for the same change in population, but the integral still varies by about 5–6%.

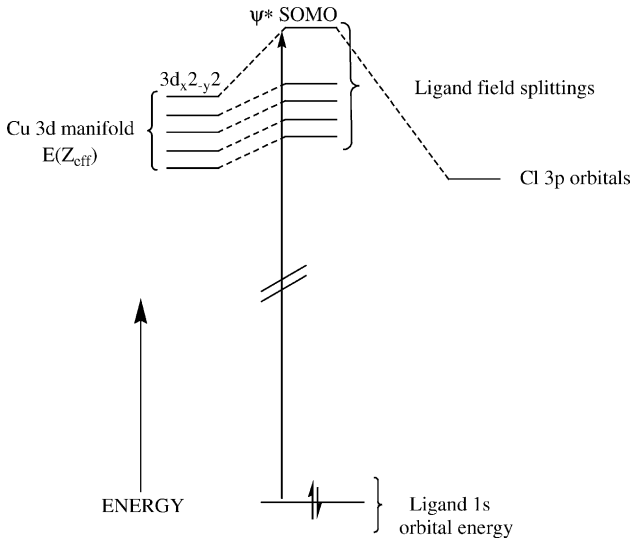

Fig. 5. Schematic representation of the contributions to the pre-edge transition energy. The pre-edge energy is determined by shifts both in the C1 1s core energy and in the energy of the HOMO of the complex. The HOMO energy is determined by overall shifts in the d-manifold related to coordination number and charge on the metal as well as the specific repulsive interaction of the HOMO determined by the ligand field of the complex.

The ligand K-edge transition generates a hole in a ligand 1s orbital. That will stabilize valence electrons on that ligand, which can lead to electronic relaxation. Electronic relaxation can be expected only if there are low lying empty orbitals of the ligand that can be populated by charge transfer from the metal in response to the excitation. But π donor ligands like Cl^- and S^{2-}/RS^- do not have low lying empty ligand orbitals for effective relaxation. For a complex like $[CuCl_4]^{2-}$ the lowest-energy unoccupied orbitals are the Cu 4s and 4p orbitals. These orbitals may provide a path for relaxation but are quite diffuse. Hartree–Fock calculations on this complex in the ground and one-electron excited states [26] showed that the metal 4s and 4p orbitals are quite high in energy, probably because of the reduced d^{n+1} final configuration. There was very little charge transfer from the metal to the ligand in the excited state, supporting the idea that electronic relaxation is not significant in ligand K-edge XAS—at least for donor ligands.

As indicated in Fig. 5, a combination of factors affects the energy position of a pre-edge transition. A shift in the core Cl 1s energy, which is related to the effective nuclear charge on the chloride, results in a change in the observed pre-edge energy. More charge donation to the metal results in a shift to deeper binding energy. In addition, the energy of the pre-edge transition is affected by the HOMO energy, which has two contributions. First, since this is mostly cen-

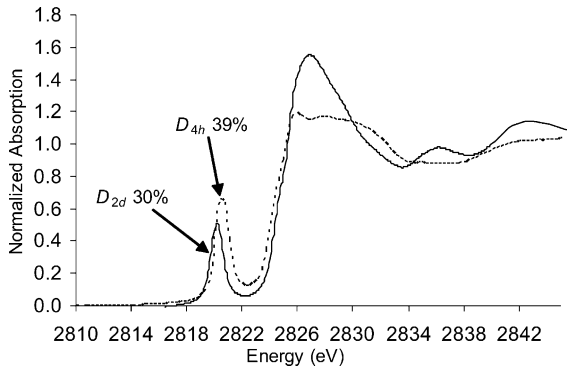

Fig. 6. Cl K-edge XAS spectra of D_{4h} (dotted) and D_{2d} (solid) $[CuCl_4]^{2-}$. The pre-edge intensity is lower for the D_{2d} complex whereas the rising edge position is higher.

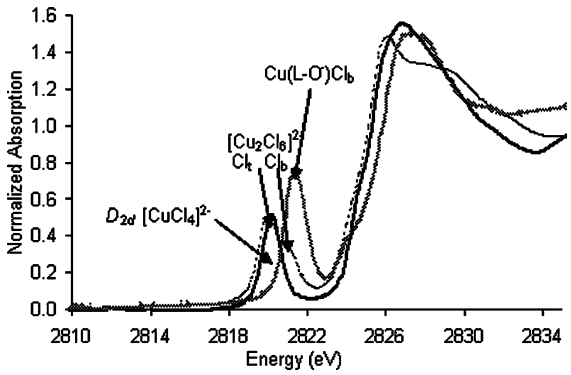

Fig. 7. C1 K-edge XAS of the monomeric complexes D_{2d} $[CuCl_4]^{2-}$ (—), dimeric distorted tetrahedral $(Ph_4P)CuC1_3$ (- - -) and $Cu(L–O^-)Cl_b$ (. . .) which has only bridging Cl ligands.

tered on the metal, the geometry of the ligand field of the complex determines the d-orbital energy splitting pattern and thus contributes to the HOMO energy. Second, the overall d-manifold can shift in energy. This is related to both the coordination number of the metal (the total antibonding and repulsive interactions with the ligands) and the effective charge on the metal, which shifts the metal orbital manifold up in energy as Z_{eff} decreases. A sum of all three effects gives the observed pre-edge energy position. The Cl 1s core shift can often be independently quantified from the energy shift in the edge transition. Ligand field contributions to the HOMO energy can be independently determined from optical d → d spectra. Correction of the observed pre-edge energy for these effects allows determination of contribution to the pre-edge energy from the energy shift of the d-manifold. This is a probe of charge donation to the metal in the complex.

3.2. Effect of geometry and bridging mode on pre-edge features

3.2.1. Change in geometry from square planar (D_{4h}) to tetrahedral (D_{2d})

Ligand K-edge spectra for D_{4h} $[CuCl_4]^{2-}$ and D_{2d} $[CuCl_4]^{2-}$ (Fig. 6) show that the intensity of the pre-edge transition for the D_{2d} complex is lower than that for the D_{4h} complex. D_{4h} $[CuCl_4]^{2-}$ has been probed by many spectral methods and is known to have 39% total Cl character in the SOMO. The intensity of the pre-edge corresponds to a 9.8% covalent contribution to the $3d_{x^2-y^2}$ HOMO per Cl in D_{4h} $[CuCl_4]^{2-}$, while from the intensity decrease of the pre-edge of D_{2d} $[CuCl_4]^{2-}$ in Fig. 6 HOMO is reduced to 7.3% per Cl. This is due to the differences in overlap between the Cl 3p orbitals and the Cu $3d_{x^2-y^2}$ orbital in the two geometries. The D_{4h} Cu $3d_{x^2-y^2}$ orbital lobes point directly at the Cl ligands, resulting in higher covalency. However the rising edge inflection point is 0.3 eV higher in the D_{2d} complex [27]. The relative energy of the rising edge inflection point indicates that the overall charge donation by the Cl in D_{2d} is greater, resulting in a Cl 1s core shift to deeper binding energy. This is also in agreement with results from a PES study [7] of these complexes, which found that D_{2d} $[CuCl_4]^{2-}$ is characterized by 3% higher Cl covalency over the d-manifold than D_{4h} $[CuCl_4]^{2-}$. Thus, even though the HOMO for the D_{4h} complex has a higher covalent contribution from Cl, the distortion from planarity in D_{2d} $[CuCl_4]^{2-}$, which results in slightly shorter bond lengths, allows a more favorable overall charge donation into unoccupied orbitals on the metal ion (i.e. 4s and 4p) and an increased bonding interaction between the Cl and the copper.

Since the effect of shifting of the Cl 1s core to deeper energy can be separately quantified from the rising edge position (0.3 eV higher for the D_{2d} complex) the differences in pre-edge energy position can be analyzed based on change in ligand field. The pre-edge transition energy is 0.4 eV lower for the D_{2d} complex relative to D_{4h} $[CuCl_4]^{2-}$. This shift is predominantly due to the effect of the ligand field change from square planar to distorted tetrahedral [53]. From optical spectra, the shift in the $3d_{xy} \rightarrow 3d_{x^2-y^2}$ transition [28,29] indicates that there is a ligand-field induced HOMO shift to lower energy in D_{2d} $[CuCl_4]^{2-}$ by 0.9 eV. Thus the combined effect of the Cl 1s orbital and ligand field energy differences should shift the pre-edge of D_{2d} $[CuCl_4]^{2-}$ down by 0.6 eV. The fact that it is experimentally observed (Fig. 6) to be shifted down by 0.4 eV requires that there is also a small energy effect of 0.2 eV attributable to a shift to higher energy of the d-manifold of D_{2d} $[CuCl_4]^{2-}$. An overall shift up in energy of the d-manifold is consistent with a slightly less positive change for the Cu ion in the D_{2d} complex due to the increased total charge donation by the Cl ligands.

3.2.2. Change in binding mode from terminal to bridging

The D_{2d} distorted tetrahedral dimer $[Ph_4P]CuCl_3$ exhibits two overlapping pre-edge features at 2820.0 and 2821.0 eV, respectively, (Fig. 7) as compared to mononuclear D_{2d} $[CuCl_4]^{2-}$ (Fig. 7) which has only one pre-edge feature at 2820.2 eV. The dimer has chlorine in two distinct binding modes, bridging (Cl_b) and terminal (Cl_t).

The two pre-edge features accordingly originate from the two chemically different chlorines. Also included is the spec-

trum of the binuclear Cu(L–O$^-$)Cl$_b$ complex (L–O$^-$ is a ligand that provides two pyridyl nitrogens and a bridging phenolate to the two coppers) which has only Cl bridging ligands. Thus the lower energy peak in the spectrum of [Ph$_4$P]CuCl$_3$ is associated with the terminal Cl ligand while the higher energy peak is from the bridging Cl ligand. The splitting is a clear indication that each Cl$_b$, bound to two coppers, donates more negative charge than each Cl$_t$, bound to only one copper. This increases the Z_{eff} of the ligand and shifts the Cl$_b$ 1s core orbital to deeper binding energy resulting in a pre-edge transition at higher energy. The lower-energy transition is hence assigned to Cl$_t$ and the higher energy to Cl$_b$ [27]. The renormalized intensity of Cl$_b$ is somewhat larger than that for Cl$_t$ (there are 2Cl$_b$/4Cl$_t$), corresponding to a covalency per Cl of 12.7 % for Cl$_t$ and 13.5% for Cl$_b$. This reflects the fact that both chlorides in the dimer are slightly more covalent with respect to the HOMO than that observed in D_{4h} [CuCl$_4$]$^{2-}$. The Cl$_t$ and Cl$_b$ pre-edge transition energies are separated by ~1 eV [27]. Because these two transitions involve the same $3d_{x^2-y^2}$ HOMO, this energy splitting provides a *direct* measure of the effect of Z_{eff} on the Cl 1s core energy due to bridging.

3.3. Extension of the methodology to d^{10-n} ($n \geq 1$) systems: Cl K-edge XAS of transition metal chlorides

Ligand K-edge XAS data of several T_d [MCl$_4$]$^{n-}$ complexes {M = Cu^{2+}, Ni^{2+}, Co^{2+}, Fe^{2+} and Fe^{3+}} were measured (Fig. 8a and b) [30]. Note that for Cu^{2+} there is one t_2 hole and the methodology for this has been discussed in Section 3.1. Ni^{2+} and Co^{2+} have two and three t_2 holes, respectively, while for Fe^{2+} and Fe^{3+} there are three t_2 and one or two e$_2$ holes contributing to the pre-edge transition (Fig. 8). The intensity and energy positions of the pre-edge and the primary 1s → 4p rising edge feature are given in Table 1. The energy position of the rising edge reflects the charge on the Cl$^-$ as the core 1s orbitals will be at deeper energy in a complex having higher Cl Z_{eff}. As discussed in Section 3.2.1, the pre-edge energy positions of these transition metal complexes provide a direct measure of their relative d orbital energies. For the complexes having same formal charge on the metal ion and similar ligand field, the relative position of the d manifold shows their

Table 1
Chlorine K-edge XAS derived MCl$_4^{n-}$ pre-edge intensities and energy positions

Complex	Pre-edge energy (eV)	Pre-edge intensity	Rising edge inflectrion point (eV)
[CuCl$_4$]$^{2-}$	2820.2	0.526	2825.4
[NiCl$_4$]$^{2-}$	2821.5	0.428	2825.0
[CoCl$_4$]$^{2-}$	2822.5	0.419	2825.0
[FeCl$_4$]$^{2-}$	2823.1	0.427	2825.0
[FeCl$_4$]$^-$	2820.8	1.505	2826.0

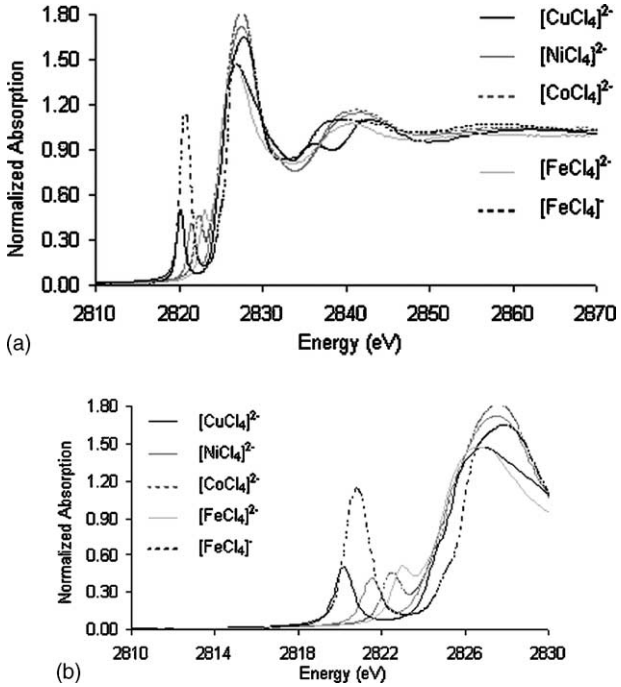

Fig. 8. (a) Cl K-edge XAS spectra of transition metal tetrachlorides Cu^{2+} (—), Fe^{3+} (- - -), Ni^{2+}(. . .), Co^{2+} (-·-·-) and Fe^{2+} (· · ·). (b) enlarged pre-edge region.

relative Z_{eff}, with Fe^{2+} < Co^{2+} < Ni^{2+} < Cu^{2+}, a trend well known from periodicity considerations, experimentally demonstrated in Fig. 8.

3.3.1. Covalency from the pre-edge intensity

In this section the methodology will be described which relates the pre-edge transition intensity to covalency for these T_d transition metal chloride systems having more than one hole.

3.3.1.1. Group theory prediction of allowed excited states in the strong field limit. To assign the transitions in systems with more than one hole, multiplet effects must be considered. The one-electron excited final states have a ligand hole and a d^{n+1} metal ion, where an electron has been excited to a metal t_2 or an e orbital from a ligand 1s (a_1 or t_2 ligand SALC's) orbital. A proper description of the excited state can be obtained by coupling the metal d^{n+1} and ligand 1s states. Table 2 gives the electric-dipole allowed excited states for each complex in the strong field limit.

3.3.1.2. Dipole strength expressions in the strong field limit. Dipole strength (D_0) for a many hole state can be expressed as

$$D_0 = \frac{1}{3N}\sum_{\alpha\beta} |\langle A\alpha|\boldsymbol{r}_i|B\beta\rangle|^2 \quad (9)$$

where A and B are many electron ground and excited states, N is the number of holes, $\boldsymbol{r}_i$ is the electric dipole operator,

Table 2
Ground states and group theoretically-allowed excited states for $[MCl_4]^{n-}$ pre-edge transitions

Complex	Ground d^n	Ground configuration (holes)	Ground state	Excited configuration (holes)	Parent d^{n+1} excited state	Allowed excited state (from ligand $a_1 + t_2$)
$[CuCl_4]^{2-}$	d^9	t_2	$^2T_2$	t_2^0	$^1A_1$	$^2A_1 + {}^2T_2$
$[NiCl_4]^{2-}$	d^8	t_2^2	$^3T_1$	t_2^1	$^2T_2$	$^3T_2 + {}^3E + {}^3T_1 + {}^3T_2$
$[CoCl_4]^{2-}$	d^7	t_2^3	$^4A_2$	t_2^2	$^3T_1$	$^4T_1 + {}^4T_1$
$[FeCl_4]^{2-}$	d^6	et_2^3	^5E	$t_2^3 + et_2^2$	$^4A_2$ $^4T_2$ $^4T_1$	$^5T_1$ $^5T_2 + {}^5T_1 + {}^5T_2$ $^5T_1 + {}^5T_1 + {}^5T_2$
$[FeCl_4]^{-}$	d^5	$e^2t_2^3$	$^6A_1$	$et_2^3 + e^2t_2^2$	^5E $^5T_2$	$^6T_2$ $^6T_2 + {}^6T_2$

Table 3
Symmetry-adapted one-electron wavefunctions for a T_d molecule

Ligand 1s orbital	SALC's	
a_1	$1/2(s_1 + s_2 + s_3 + s_4)$	
$t_2(x)$	$1/2(s_1 - s_2 + s_3 - s_4)$	
$t_2(y)$	$1/2(s_1 + s_2 - s_3 - s_4)$	
$t_2(z)$	$1/2(s_1 - s_2 - s_3 + s_4)$	
Metal d type orbitals	SALC's	Ligand component
$e(\theta)$	$\sqrt{(1-c_3^2)}d_{z^2}$	$+c_3[1/2(p_{x'1} - p_{x'2} - p_{x'3} + p_{x'4})]$
$e(\epsilon)$	$\sqrt{(1-c_3^2)}d_{x^2-y^2}$	$+c_3[1/2(p_{y'1} - p_{y'2} - p_{y'3} + p_{y'4})]$
$t_2(x)$	$\sqrt{[1-(c_1^2+c_2^2)]}d_{yz}$	$+c_1[1/2(p_{z'1} - p_{z'2} + p_{z'3} - p_{z'4}] + c_2[1/4(p_{x'1} + p_{x'2} - p_{x'3} - p_{x'4}] + \sqrt{3}(-p_{y'1} - p_{y'2} + p_{y'3} + p_{y'4})$
$t_2(y)$	$\sqrt{[1-(c_1^2+c_2^2)]}d_{xz}$	$+c_1[1/2(p_{z'1} + p_{z'2} - p_{z'3} - p_{z'4})] + c_2[1/4(p_{x'1} - p_{x'2} + p_{x'3} - p_{x'4})] + \sqrt{3}(p_{y'1} - p_{y'2} + p_{y'3} - p_{y'4})$
$t_2(z)$	$\sqrt{[1-(c_1^2+c_2^2)]}d_{xy}$	$+c_1[1/2(p_{z'1} - p_{z'2} - p_{z'3} + p_{z'4}] - +c_2[1/2(p_{x'1} + p_{x'2} + p_{x'3} + p_{x'4}]$

From C.J. Ballhausen, H.B. Gray, Molecular Orbital Theory, Benjamin Press, New York, 1964, pp. 108–109.

α, i, β are components of ground state, dipole operator and excited state, respectively. The evaluation of this sum over all relevant many-electron ground and excited state wavefunctions is simplified by applying the irreducible tensor method, which uses the Wigner-Eckart theorem [31], to take advantage of the symmetry.

Each pre-edge transition integral can be expanded with respect to the components of the ground state, excited state and electric dipole operator. Some of those will be zero from group theory. The rest can be reduced to one of the following three one-electron matrix elements $\langle a_1||t_2||t_2\rangle$, $\langle t_2||t_2||t_2\rangle$ and $\langle t_2||t_2||e\rangle$ [30]. Each of these one-electron reduced matrix elements can be related to a one-electron orbital integral, $\langle \Gamma_0\Psi_0|\mathbf{r}|\Gamma_1\Psi_1\rangle$, where $|\Gamma_0\Psi_0\rangle$ and $|\Gamma_1\Psi_1\rangle$ are one-electron orbitals Ψ_0 and Ψ_1 having Γ_0 and Γ_1 symmetry, respectively. These integrals are as discussed in Section 3.1, using SALC's of ligand valence orbitals and metal orbitals in the T_d molecular framework (Table 3; the coefficients c_1 and c_2 are the σ and π ligand orbital coefficients in the t_2 molecular orbitals while c_3 is the coefficient of σ bonding in the e set of molecular orbitals).

The summation of the square of these one-electron integrals gives the dipole strength (D_0). The excited states that are related to the same d^{n+1} excited configuration, only varying in their ligand core orbital origin (a_1 or t_2), should be degenerate and their contribution to the pre-edge intensity should be additive (this assumes that the repulsion between the localized ligand core 1s electron and valence d-manifold electron is minimal). The final expressions of the dipole strengths in terms of the coefficients of the SALC's of the ligand bonding orbitals are given in Table 4. The Cu^{2+}, Ni^{2+} and the Co^{2+} complexes have only one, one-electron excited d^{n+1} parent final state (Table 2 column 6) and their dipole strength is proportional to the total 3p-σ and 3p-π

Table 4
Strong field dipole strength expressions for $MCl_4{}^{2-}$ pre-edge transiton intensities

Complex	Parent d^{n+1} excited state	Dipole strength for transition to parent excited state
$[CuCl_4]^{2-}$	$^1A_1$	$(1/3)(c_1^2 + c_2^2)\boldsymbol{R}^2\langle s|\boldsymbol{r}|p\rangle^2$
$[NiCl_4]^{2-}$	$^2T_2$	$(2/3)(c_1^2 + c_2^2)\boldsymbol{R}^2\langle s|\boldsymbol{r}|p\rangle^2$
$[CoCl_4]^{2-}$	$^3T_1$	$(c_1^2 + c_2^2)\boldsymbol{R}^2\langle s|\boldsymbol{r}|p\rangle^2$
$[FeCl_4]^{2-}$	$^4A_2$	$(1/3)c_3^2\boldsymbol{R}^2\langle s|\boldsymbol{r}|p\rangle^2$
	$^4T_2$	$(1/2)(c_1^2 + c_2^2)\boldsymbol{R}^2\langle s|\boldsymbol{r}|p\rangle^2$
	$^4T_1$	$(1/2)(c_1^2 + c_2^2)\boldsymbol{R}^2\langle s|\boldsymbol{r}|p\rangle^2$
$[FeCl_4]^{-}$	^5E	$(2/3)c_3^2\boldsymbol{R}^2\langle s|\boldsymbol{r}|p\rangle^2$
	$^5T_2$	$(c_1^2 + c_2^2)\boldsymbol{R}^2\langle s|\boldsymbol{r}|p\rangle^2$

Table 5
Distribution of energies and intensities for final states of MCl_4^{2-} pre-edge transitions

T_d metal ion	Parent d^{n+1} excited state	Higher state of approximate symmetry for mixing	Relative energy value (eV)	Coefficient of mixing	Theoretical intensity ratios
Co^{II}	$^3T_1$		0.0	0.84	1
		$^3T_1$	1.66	0.16	0.19
Fe^{II}	$^4A_2$		−0.31		0.42
	$^4T_2$		0.0		1
	$^4T_1$		0.23	0.29	0.29
		$^4T_1$	1.42	0.71	0.71
Fe^{III}	^5E		0.0		0.58
	$^5T_2$		0.49		1

character in their t_2 orbital ($c_1^2 + c_2^2$) times the number of holes in the t_2 orbital in the ground state in each case. Fe^{2+} and Fe^{3+} have more than one possible d^{n+1} parent excited state (Table 2 column 6), and the total intensity which now includes transition to one or two e holes (c_3^2) is distributed over these multiplets.

3.3.1.3. The effects of intermediate ligand fields, i.e. mixing with higher excited states. The above description has assumed a strong ligand field limit for these complexes. However, in T_d complexes the ligand field is relatively weak, which can lead to mixing of the allowed parent excited final state with high energy states of the same symmetry corresponding to excitation of more than one-electron. This will lead to redistribution of edge intensity to these high energy states. The direct consequence of this will be a decrease in observed experimental pre-edge intensity as the higher energy states overlaps with the rising edge, and thus shifts intensity out of the pre-edge. The extent of this mixing can be quantitatively estimated using the d^{n+1} Tanabe-Sugano matrices. The Fe^{2+} and Co^{2+} case has significant mixing of the allowed T_1 states with higher energy $^4T_1$ (71%) and $^3T_1$ (16%) excited states, respectively (Table 5).

3.3.1.4. Determination of covalency from experimental intensity. The pre-edge intensities of these complexes should ideally show an intensity ratio of 1:2:3:4:5 reflecting the increasing number of holes from Cu^{2+} to Fe^{3+}. Fig. 9 shows the experimental fits for the complexes. For Cu^{2+} and Ni^{2+} (Fig. 9a and b) a single transition contributes to the pre-edge and the observed pre-edge intensity (Table 1) is the total multiplet intensity. Their intensities are approximately equal and this deviation from the expected 1:2 trend reflects decrease in chloride bonding due to the decrease in metal Z_{eff} (decreasing covalency) for Ni^{2+} relative to Cu^{2+}. In case of Co^{2+} (Fig. 9c) the experimentally observed pre-edge is also due to a single d^{n+1} final state, however, the intensity is 84% of the total multiplet intensity due to mixing with higher-energy allowed $^3T_1$ state and hence has to be scaled up appropriately. The total intensity is again similar to that of Cu^{2+} even though three holes are involved reflecting a further decrease in covalency relative to Ni^{2+}. In Fe^{2+} and Fe^{3+} (Fig. 9d and e) there are more than one contributing multiplet state and transitions to (e) as well as t_2 orbitals. These transitions are not equally intense due to differences between π and σ covalencies. Additionally, Fe^{2+} has mixing with a higher-energy two-electron excited states (as with Co^{2+}) and hence the observed transition intensity has to be rescaled (resulting in an increase).

To extract the orbital coefficients of Cl 3p orbitals (c_i^2's in Table 5) we need an estimate of $\langle \mathbf{r} \rangle_{1s,3p}$. These coefficients of the ground state wave function of D_{4h} $[CuCl_4]^{2-}$ are known from various spectroscopic techniques [8]. Compared to the D_{4h} $[CuCl_4]^{2-}$ results, the total Cl contribution to the SOMO of D_{2d} $[CuCl_4]^{2-}$ (Fig. 5) is 30%. The $\langle \mathbf{r} \rangle_{1s,3p}$ for D_{2d} $[CuCl_4]^{2-}$ complex was experimentally obtained from its pre-edge intensity (Section 3.2.1). Using this value, the percentage covalency of other $[MCl_4]^{n-}$ is determined (Table 6 1st column). As discussed above, the effect of change of charge on the radial integral $\langle \mathbf{r} \rangle_{1s,3p}$ is insignificant. Note that the numbers in Table 6 give the covalency of the t_2 orbitals for Cu^{2+}, Ni^{2+} and Co^{2+} and also include 1/3rd and 2/3rd of the covalency of the e π orbitals in Fe^{2+} and Fe^{3+}, respectively.

3.3.1.5. Correlate to DFT calculations. SCF-Xα calculations were performed on D_{2d} $[CuCl_4]^{2-}$ and T_d $[MCl_4]^{n-}$ [where M = Ni^{2+}, Co^{2+}, Fe^{2+}, Fe^{3+}] [30], to compare with the results obtained from ligand K-edge XAS. The results of the calculations are also included in Table 6. The total Cl 3p character, summed over all four Cl ligands in each hole that contributes to the pre-edge intensity varies from 28% in $[CuCl_4]^{2-}$ to 10% in $[FeCl_4]^{2-}$. This correlates well with the observed decrease in covalency, d-orbital energy and reduction in Z_{eff} of the metal. $[FeCl_4]^-$ has 22% Cl 3p compared to 10% in $[FeCl_4]^{2-}$ reflecting the increase in oxidation state (i.e. Z_{eff}) of the former and associated change in bond length.

3.4. DFT calculation methods

Kohn–Sham molecular orbitals from density functional calculations [32] can be analyzed by various population methods to quantify metal ligand bond covalencies. While

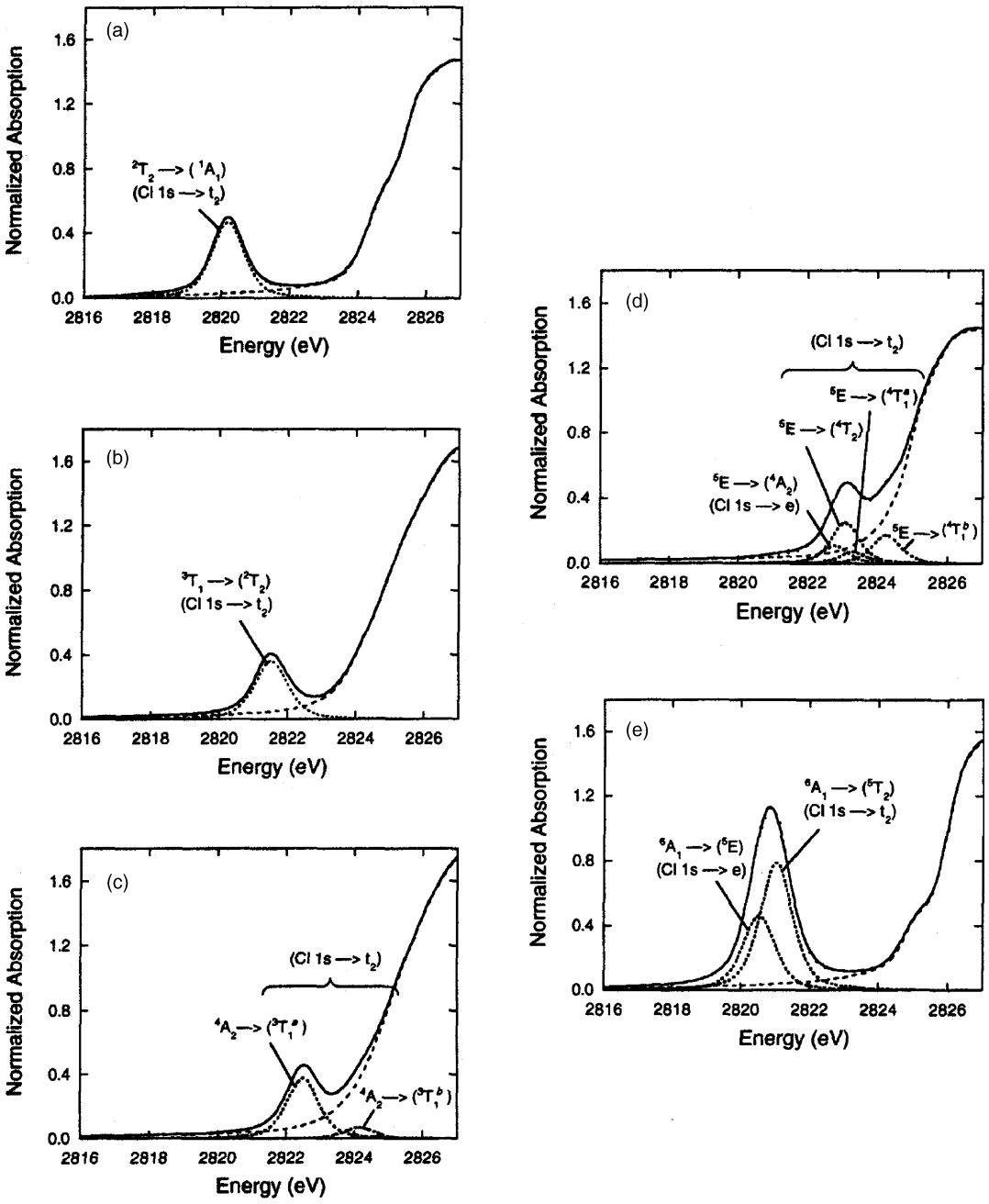

Fig. 9. Pre-edge transition assignments for (a) $[CuCl_4]^{2-}$, (b) $[NiCl_4]^{2-}$, (c) $[CoCl_4]^{2-}$, (d) $[Fe^{II}Cl_4]^{2-}$ and (e) $[Fe^{III}Cl_4]^{-}$. The transitions are fixed to theoretical intensity and energy splittings, and are designated by the ground state of each system and the parent d^{n+1} metal excited state to which the transition occurs. States designated by (b) denote the excited states that derive intensity due to CI mixing.

Table 6
Summary of experimentally observed covalency and results of SCF-Xα-SW calculations of $[MCl_4]^{n-}$ complexes

T_d complex	Experimental Cl 3p character observed in total multiplet intensity per hole (%)	Calculated Cl 3p character in metal d-derived orbitals per hole (%)	Calculated Cl 3p character in total multiplet intensity per hole (%)
$[CuCl_4]^{2-}$ (D_{2d})	30.0 ($= c_1^2 + c_2^2$)	28.2 ($= c_1^2 + c_2^2$)	28.2
$[NiCl_4]^{2-}$	11.8 ($= c_1^2 + c_2^2$)	16.7 ($= c_1^2 + c_2^2$)	16.7
$[CoCl_4]^{2-}$	9.0 ($= c_1^2 + c_2^2$)	12.3 ($= c_1^2 + c_2^2$)	12.3
$[FeCl_4]^{2-}$ (t_2)	11.9 ($= c_1^2 + c_2^2 + (1/3)c_3^2$)	10.2 ($= c_1^2 + c_2^2$)	12.4 ($= c_1^2 + c_2^2 + (1/3)c_3^2$)
(e)		6.5 ($= c_3^2$)	
$[FeCl_4]^{-}$ (t_2)	29.8 ($= c_1^2 + c_2^2 + (2/3)c_3^2$)	22.4 ($= c_1^2 + c_2^2$)	35.3 ($= c_1^2 + c_2^2 + (2/3)c_3^2$)
(e)		19.3 ($= c_3^2$)	

these methods can differ significantly in determining the total atomic charges, they show limited method dependence in atomic spin densities or electron hole covalencies when employing a theoretically converged basis set. The electron hole covalency, as the reflection of the nature of the uncompensated electron density of the bonding orbital combinations, hence the ground state bonding description and the spin density, were found to be similar to each other with at most 7% difference for Cu^{2+} complexes [33]. These wave function properties can be directly correlated with EPR, ENDOR, ESEEM (electron spin density) and XAS edge (SOMO hole covalency) spectroscopies.

The major difference between the computational methods is the way the electron density is distributed among the nuclear centers. The Mulliken population analysis [34] equally distributes the electron density, while the Bader's atoms-in-molecules (AIM) method [35] uses the topology of the electron density and divides it up along the zero-flux surfaces. Weinhold's natural population analysis [36] uses a set of core, valence and Rydberg natural orbitals to fit the electron density. It is worth noting that inclusion of the transition metal 4p orbitals into the valence set can significantly influence the results of the population analysis [37]. The latter two methods are available for electronic structure calculations with Gaussian-type basis sets. Alternative methods are available for analyzing results obtained with Slater-type basis sets. The Voronoi method [38] is somewhat similar to the AIM method and partitions the space into non-overlapping atomic areas, called the Voronoi cell, which is the region in space closer to a given nucleus than to any other nuclei. The Hirschfeld [39] population analysis employs well-defined fragments to describe the electron density, which is shared by several atoms in proportion to their free-atom densities and the integration of the bonded minus free-atom densities defines the net atomic or orbital charges.

In general, all population analysis methods can give reasonable agreement with experimentally determined orbital covalencies as the method dependence of the spin densities and hole populations (4 and 2%, respectively for Cu^{2+} complexes) is negligibly small employing a theoretically converged basis set. In general, the natural population analysis method tends to give more accurate results than the Mulliken method, while the application of atoms-in-molecule method, which is considered as one of the most accurate approaches for dividing electron density between atoms, can be limited by the highly complex nature of the electron density of larger complexes. Methods utilizing the results of calculations of Slater-type basis sets are equally reliable and give comparably good results as the AIM.

4. Cu–S protein sites

The copper sites in biological systems involved in electron transfer all have thiolate ligands (i.e. Cu–S(cysteine) bonds), which play a critical role in the unique physical properties of these sites and their function [40]. Those containing mononuclear sites are the blue copper proteins (azurin, plastocyanin, etc.). These all have a distorted tetrahedral structure with a short Cu–S(thiolate) bond (∼2.1 Å), long axial Cu–S(thioether) bond (∼2.9 Å) and two fairly normal Cu–N(histidine) bonds (Fig. 10A) [41]. Within the blue copper series, there are a number of proteins were the axial ligand is varied (nitrite reductase with a short Cu–S(thioether) bond at ∼ 2.6 Å [42], stellacyanin with a Cu–O(carbonyl) bond at ∼2.1 Å [43], and fungal laccase [44] with no axial ligand). An interesting question has been the role of the axial ligand in the properties and reactivities of the blue copper site. Generally, the blue copper sites have intense absorption bands in the visible spectral region [45], which are assigned as thiolate to Cu(II) charge transfer bands, and a very small copper hyperfine coupling in their EPR spectra. The low energy and high intensity of the charge transfer transitions and the small hyperfine coupling are associated with the highly covalent Cu–S(Cys) bond, which has been extremely important to understand as this is the redox active molecular orbital (RAMO) involved in the long-range electron transfer function of these proteins. DFT calculations as early as 1985 [3] showed the RAMO (Fig. 10B), as defined by the spin unrestricted β-LUMO of the Cu(II) form, to be perpendicular to the long axial Cu–S(thioether) bond (also found experimentally from single crystal EPR [46]) and highly covalent with the dominant covalency involving the S 3p π orbital of the thiolate. This covalency was extremely important to evaluate experimentally, as was the effect of the axial ligand variation on this bond.

The binuclear copper electron transfer center, Cu_A, is found in nitrous oxide reductase and cytochrome *c* oxidase [47–50,62]. This site has two coppers bridged by two thiolate ligands forming a [2Cu–2S] diamond core. In addition to the bridging thiolates, each copper has an approximately equatorial His nitrogen and axial Met sulfur or backbone carbonyl oxygen ligands (Fig. 11) [51]. During redox, these sites change from [Cu(I)Cu(I)] to [Cu(II)Cu(I)], where the latter is a completely delocalized, class III mixed-valent system. It is important to note that Tolman and co-workers have synthesized [52] a binuclear copper model system that is also a class III mixed-valent (MV) model, but with the Cu–Cu distance increasing from 2.5 Å in Cu_A to 2.9 Å in the model. From calculations, Cu_A has a σ type LUMO (Fig. 11B) while the MV model complex has a π type LUMO (Fig. 11C). For the Cu_A center, it has been important to define the covalency of the copper bonds with the bridging thiolate sulfurs, its contribution to electron delocalization between the coppers and how the electron delocalization affects the redox properties of Cu_A, including its covalent coupling through the thiolates into the protein superexchange pathways.

The natures of the ground state wave functions of both the blue copper and Cu_A centers have been elucidated by sulfur K-edge XAS.

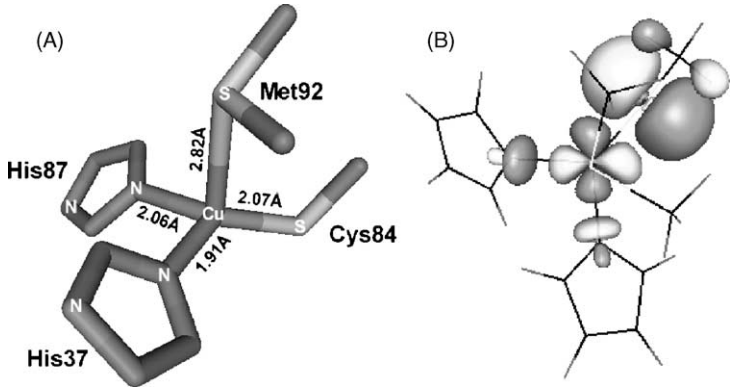

Fig. 10. Molecular structure (A) and redox active MO (B) of oxidized poplar plastocyanin [49] active site.

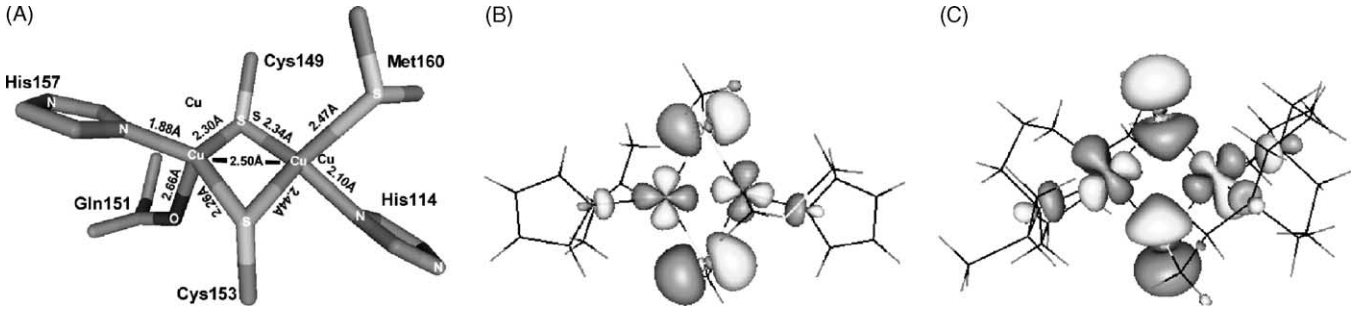

Fig. 11. Molecular structure (A) and redox active MO (B) of the Cu_A active site from *Thermus thermophilus* [69] along with the redox active MO (C) of the binuclear model complex [52,142].

4.1. Blue Cu site

The S K-edge spectra [53] of the blue Cu site in poplar plastocyanin and a Cu(II)–thiolate model compound [Cu(S–C_6H_4–*o*–CO_2) (tet b)] with a normal Cu(II)–S(thiolate) bond length of 2.36 Å are shown in Fig. 12B with the associated S 1s → LUMO orbital diagram given in Fig. 12A. The energy position of the pre-edge in the model complex is about 1.3 eV higher than for plastocyanin, which indicates a difference in the copper Z_{eff} which is lower for Cu-tet b. The Cu-tet b model [54] has a distorted five-coordinate geometry, which destabilizes

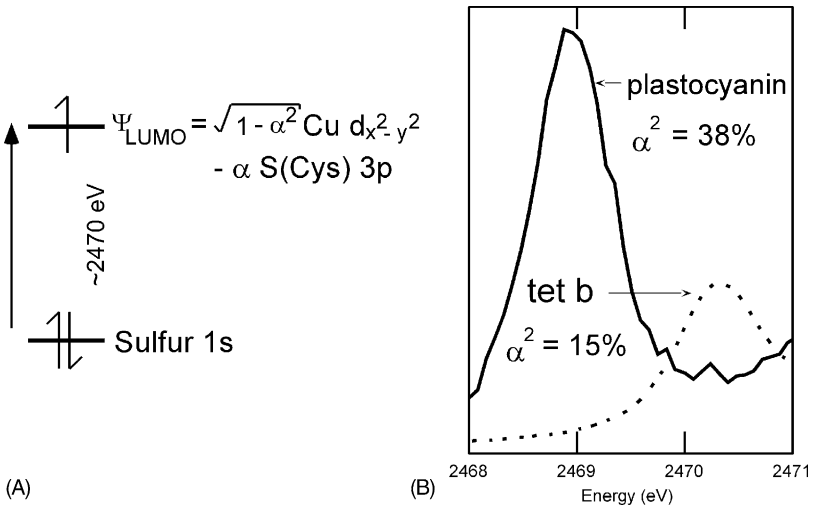

Fig. 12. Energy level diagram depicting S 1s → LUMO transition (A) and renormalized S K-edge XAS spectra of plastocyanin (solid line) and Cu-tet b, a model complex (dashed line).

the Cu 3d-manifold relative to the plastocyanin active site, which has a four-coordinate Cu(II) with a weakly bound axial thioether. This energy difference also appears in their absorption spectra [46,54,55] as the charge transfer band shifts to higher energy by 1.4 eV going from a four- to five-coordinate site. In addition, the pre-edge intensity for plastocyanin is nearly three times higher than that of the Cu-tet b model complex, after renormalization of the protein spectrum (Fig. 12B). The quantitative analysis of the pre-edge intensities gives 15% S 3p character in the LUMO of the model complex and consequently 38% S 3p character for plastocyanin. This large ligand character of the LUMO directly reflects the high covalency of the Cu(II)–S(Cys) bond in the blue copper site.

GGA and hybrid DFT calculations give a ground state bonding description in qualitative agreement with experiment. The bonding between the Cu(II) and S(Cys) is pure π-type and the LUMO is based on Cu $3d_{x^2-y^2}$ and S(Cys) 3p orbitals. The axial S(Met) does not contribute to the ground state wavefunction. However, the covalency of the Cu(II)–S(Cys) bond shows a strong functional dependence (Table 7). The pure DFT or GGA calculation employing the BP86 functional and a theoretically converged basis set (BS5 [56]) overestimates the S 3p character of the LUMO by 10%, as calculated by Weinhold's Natural Population Analysis [37,57,58]. The hybrid B3LYP functional [59–61] with 20% Hartree–Fock exchange only slightly improves the covalency value. The spectroscopically adjusted hybrid functional B(38HF)P86 developed for the $[CuCl_4]^{2-}$ complex [56] gives reasonable agreement with the experimental S 3p character, as well as with Cu L-edge results [12]. The total ground state wavefunction of the blue Cu site can be defined by 46% S(Cys), 42% Cu, 9% His, and 3% α-methylene H contributions (Table 7) showing highly anisotropic covalency along the Cu(II)–S(Cys) bond.

A recent study [63] of axial ligand variants in a fixed protein environment has clearly shown the effect of the axial ligand on the ground state wave function of the blue Cu site. Fig. 13A shows the S K-edge spectra of wild-type, Q99M and Q99L variants of cucumber stellacyanin, where the axial ligands are O from a glutamate, S from a methionine and none from a leucine residue, respectively. In the same order, the pre-edge intensity increases (from 41 to 47% and to 54% S 3p for WT, Q99M and Q99L variants, respectively) indicating an increasingly more covalent Cu(II)–S(thiolate) interaction. These results parallel EXAFS and resonance Raman data [63], which show shortening of the Cu(II)–S(thiolate) bond and increase in the Cu(II)–S(thiolate) stretching frequencies as the axial interaction weakens (Fig. 13B).

Table 7
Atomic spin densities and orbital populations by means of Natural population analyses for the plastocyanin computational model complex $[Cu(SMet)(imidazole)_2(SMet_2)]^{1+}$

	Cu	S(Cys)	C(Cys)	H(Cys)	N(His)
Spin density					
BP86/BS5	28	58	−1	3	11
B3LYP/BS5	32	57	−1	3	10
B(38HF)P86/BS5	41	50	−1	3	10
Experimental				2[a]	8[b]
LUMO					
BP86/BS5	30	55	1	3	10
B3LYP/BS5	34	54	0	2	8
B(38HF)P86/BS5	41	49	0	2	7
Experimental	41[c]	45[d]			

[a] Paramagnetic NMR [138] + 1% contribution from C(Cys).
[b] ^{14}N ENDOR [139] + 1% from other ring atoms.
[c] Cu 3d character by Cu L-edge XAS for plastocyanin [30] + 1% Cu 4s/4p contribution.
[d] S 3p character by S K-edge XAS for azurin [21] + 1% S 3s contribution.

4.2. Cu_A site

The renormalized S K-edge spectrum [64] of the engineered Cu_A site in *Pseudomonas aeruginosa* azurin [51] is shown in Fig. 14. The pre-edge energy of the Cu_A site is about 0.9 eV higher than that for plastocyanin. This can be rationalized by a higher Z_{eff} on a bridging thiolate-S in Cu_A relative to a terminal thiolate-S in plastocyanin and an additional contribution from the Cu–Cu bonding (see below), which destabilizes the Cu 3d-manifold giving a pre-edge feature at higher energy. The pre-edge intensity of the Cu_A

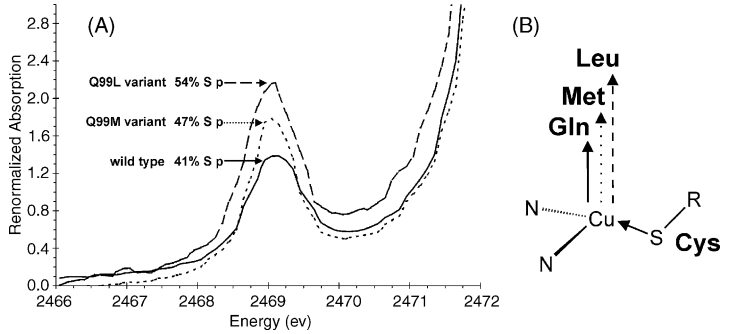

Fig. 13. Comparison of S K-edge spectra of wild-type (—) cucumber stellacyanin and its Q99M (···), Q99L (- - -) variants (A) and the coupled distortion model (B).

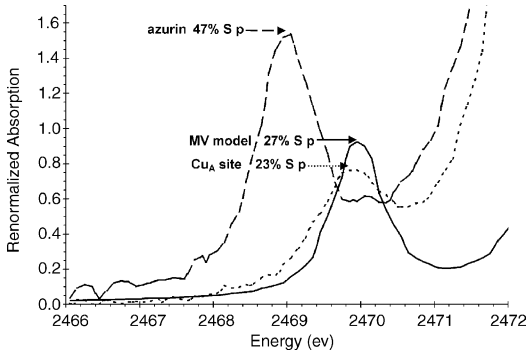

Fig. 14. Renormalized S K-edge XAS spectra of the Cu_A azurin construct (···), a mixed-valence model (—) and azurin (- - -).

site is quantified to be 23% per S atom using the thiolate-S transition dipole integral (estimated above for Cu-tet b/blue Cu), which gives a total LUMO covalency of 46%. Note that the intensity is reduced relative to plastocyanin, since there is one Cu $3d_{x^2-y^2}$ hole per two thiolates for the MV state of Cu_A, while plastocyanin has one hole per thiolate. In comparison to the blue Cu site, the Cu_A site has similar Cu and S characters, however, these are delocalized over the two Cu and two S centers, which has importance in its ET function.

Fig. 14 also includes the S K-edge spectrum [64] of the mixed-valence model complex (MV complex [52]), which shows the pre-edge feature at similar energy and intensity as found for the Cu_A site. However, from MCD studies [65], the $\sigma \rightarrow \sigma^*$ transition energies and therefore the interaction between the $3d_{x^2-y^2}$ orbitals in the two copper centers (i.e. the electronic coupling matrix element, $H_{Cu–Cu}$) of Cu_A and the MV model were found to be very different: $2H_{Cu–Cu} = 13{,}000$ and $5600\ cm^{-1}$, respectively. The similar pre-edge intensities, corresponding to 46 and 54% S character in Cu_A and the MV model, rules out the possibility that a superexchange interaction through the Cu–S–Cu bonds is the origin for the difference in $H_{Cu–Cu}$. Therefore, the $\psi \rightarrow \psi^*$ transition energy difference must reflect the direct overlap of the two Cu $3d_{x^2-y^2}$ orbitals via a Cu–Cu bond in Cu_A. As shown in Fig. 11B and C, this originates from the rotation of the Cu 3d orbitals in Cu_A relative to the MV model and gives a stronger, σ-type overlap in the Cu_A site (relative to the π interaction through the bridging thiolate in the MV model), which corresponds to a larger σ/σ* gap and therefore higher $H_{Cu–Cu}$ value.

As with the blue Cu site, density functional calculations allow definition of the total ground state wavefunction. The hybrid B3LYP functional gives a reasonable ground state wave function for the mixed-valence state of the Cu_A active site with >94% delocalization over the two coppers (the ratio of spin densities of the two coppers are 46%:54%) [66]. The ground state is characterized by σ interactions between the Cu $3d_{x^2-y^2}$ orbitals (Fig. 11B) and mixed σ- and π-type bonding between the S 3p and Cu $3d_{x^2-y^2}$ orbitals. As shown in Table 8, the total ground state wavefunction can be defined as 45% Cu, 47% S(Cys), 6% His, 3% α-methylene

Table 8
Atomic spin densities and orbital populations by means of natural population analyses for the Cu_A computational model complex $[Cu_2(SMet)_2(imidazole)_2(SMet_2)(OC(Met)(CHNH_2)]^{1+}$ using the B3LYP hybrid functional with BS5

	Cu^S/Cu^O	S^S/S^O(Cys)	H^S/H^O(Cys)	N^S/H^O(His)
Spin density				
Calculated	19/23	21/31	1/1	2/3
Experimental			3[a]	6[b]
LUMO				
Calculated	21/23	20/30	0/0	2/1
Experimental	44[c]	46[d]		

Superscripts S and O indicate atoms closer to the Met and Gln axial ligands, respectively.
[a] Paramagnetic NMR [140].
[b] ^{14}N ENDOR [140,141].
[c] Cu 3d character by Cu L-edge XAS [72] + 1% Cu 4s/4p contribution.
[d] S 3p character by S K-edge XAS [72] + 1% S 3s contribution.

H. Table 8 also shows the Cu 4s/4p and S 3s contributions to define the total electron hole (coefficients sum to 100%) as derived from B3LYP calculations scaled to experiment. The axial Met and carbonyl ligands do not contribute to the ground state wave function.

4.3. Functional relevance of the Cu(II)–S(Cys) covalent bond

Since the rate of ET is proportional to the electronic coupling-matrix element (H_{DA}) between the donor and acceptor partners in ET and hence to α^2 [67], the high anisotropic covalency along the Cu(II)–S(Cys) bond corresponds to a large H_{DA} activating an efficient ET pathway through the Cys residue.

In blue Cu proteins, there are two sites for the intramolecular ET pathway (Fig. 15A) [41,68]. The adjacent site is only ∼5 Å from the Cu atom and it is assumed to be the input pathway through a coordinating His ligand with 4% covalency. The distant site is about 13 Å away and it is connected through the Cys residue to the Cu atom. The high covalency of the Cu–S(thiolate) bond (45%) is essential for efficient ET along such a long distance (9–11 covalent bonds) to the remote Tyr site. This results in similar ET rates for both the adjacent and remote sites [13].

S K-edge and Cu L-edge spectroscopies reveal similar covalencies in the binuclear Cu_A sites relative to the blue Cu sites. However, this covalency is equally distributed between the two Cu atoms. This delocalization contributes to lowering the inner-sphere reorganization energy of the Cu_A site by approximately a factor of two relative to the blue Cu site, which according to Marcus theory [69,70], increases the ET rate by nearly an order of magnitude. In addition, the bridging Cys ligands provide multiple input and output pathways as summarized in Fig. 15B. Based on pathway simulations [64], the most plausible input pathway from the cytochrome *c* is through the exposed bridging Cys ligand, while at least three possible output pathways were identified

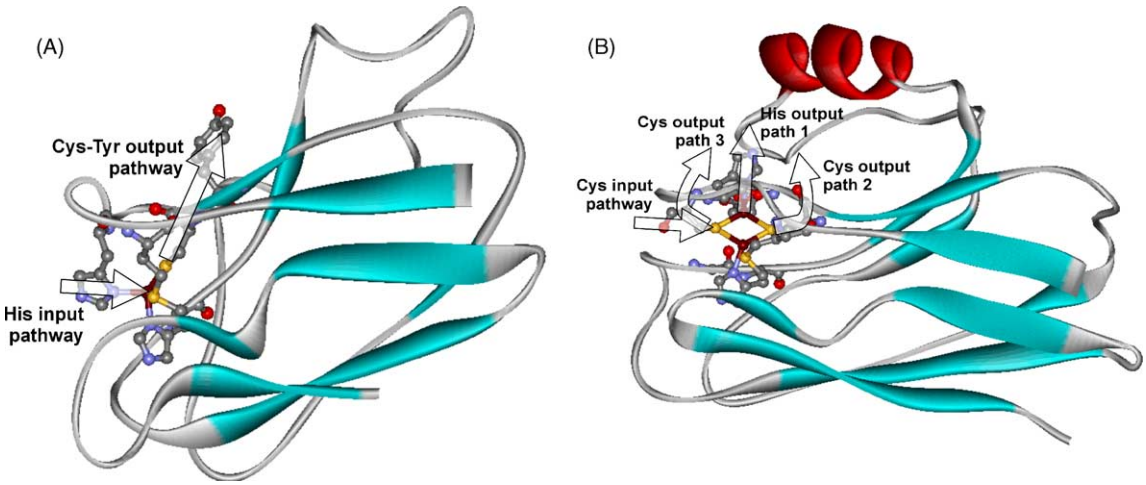

Fig. 15. Electron transfer pathways in blue Cu (A) and Cu_A (B) metalloproteins.

connecting the Cu_A site with the distant heme *a* site. The 26% covalency per Cys ligand makes the cysteine pathway competitive with the shorter histidine pathway with only 3% covalency for the latter.

5. Ligand K-edge XAS of iron–sulfur active sites and their model complexes

5.1. Mononuclear iron–sulfur models of rubredoxins

The simplest of the iron–sulfur active sites is found in the rubredoxins. They are small (9–11 kDa) proteins having one iron atom coordinated to four thiolate sulfurs of four cysteine residues with a distorted tetrahedral geometry (Fig. 16a). The iron atom in the active site exists in high spin ferric and ferrous forms in its oxidized and reduced states, respectively. These occur widely in nature and are known to perform single electron transport. Their small size and stability at room temperature make the rubredoxins relatively easy to study. There are at least 47 reported crystal structures of different rubredoxins and their mutants in the Protein Data Bank enabling electronic structure calculations to be performed for the active sites of these enzymes.

5.1.1. S K-edge XAS of $[M(SR)_4]^{n-}$ [M = Fe(II), Co(II), Ni(II) and Fe(III)]

The $Cu–S_{thiolate}$ bond in plastocyanin has been analyzed in great detail as described in Section 4. This represented a system with one hole in the d manifold. Transition metal thiolates provide a good starting point for understanding the nature of the metal–thiolate bond in systems having more than one hole. S K-edge XAS of transition metal tetrathiolates was therefore performed and a methodology similar to that of metal tetrachlorides (Section 3) was developed [71]. The S K-edge XAS of $[M(SR)_4]^{n-}$ complexes, where M= Fe^{2+}, Co^{2+}, Ni^{2+} and Fe^{3+}, are shown in Fig. 17. In addition to a pre-edge feature corresponding to the S 1s to metal antibonding orbital transitions, the S K-edge XAS has a sharp feature around 2471–2472 eV, below the 1s → 4p

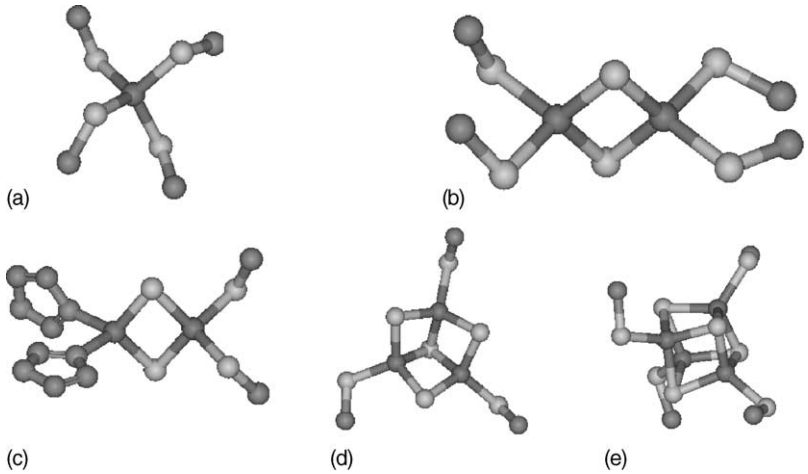

Fig. 16. Iron–sulfur clusters found in ET proteins. (a) $Fe(SCys)_4$ (rubredoxin), (b) Fe_2S_2 (plant ferredoxin), (c) Fe_2S_2 (Rieske protein), (d) Fe_3S_4 (ferredoxin II), (e) Fe_4S_4 (bacterial ferredoxin and HiPIP) (hydrogen atoms on beta-methylene groups are omitted for clarity).

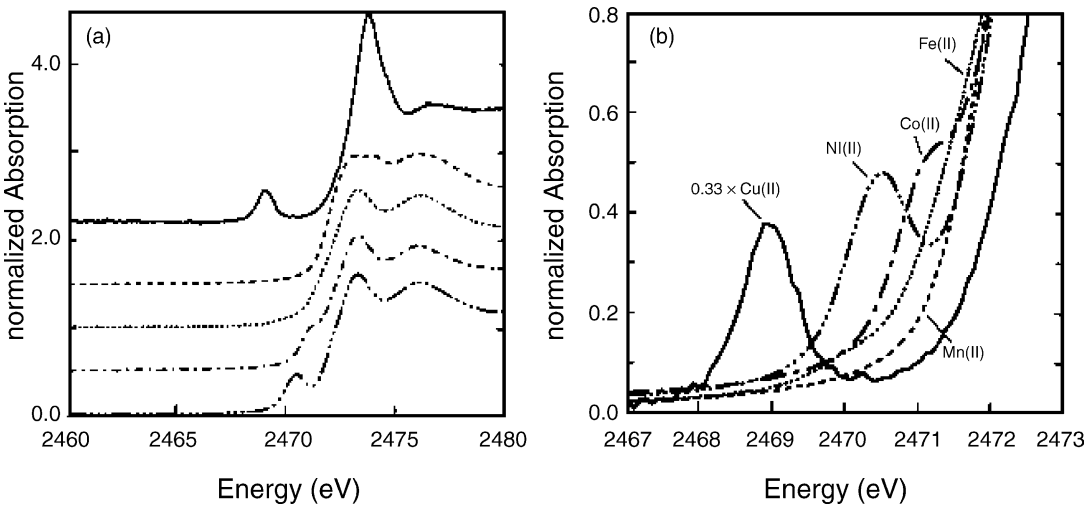

Fig. 17. (a) The S K-edge XAS spectra of $M(SR)_4^{2-}$ complexes where M = Ni^{2+} (· · ·–· · ·), Co^{2+} (·–·–·), Mn^{2+}(- - -) and Fe^{2+} (· · ·). The plastocyanin pre-edge (scaled) representing Cu^{2+} (—) is shown for reference. (b) Pre-edge in expanded scale.

transition at around 2475 eV. This was assigned as the S 1s → ligand C–S σ* transition [71]. The energy of the pre-edge position reflects the effect of the metal Z_{eff} on its d-orbital energies. In the case of Fe^{2+} and Mn^{2+}, the Z_{eff} is relatively low and thus the pre-edge transition is at a higher energy and not resolved as it overlaps the C–S σ* transition feature.

As discussed for the tetrachlorides in Section 3, the parent excited states were calculated in each case assuming S_4 site symmetry to evaluate the multiplet contribution to the pre-edge intensity. The Cu–S bond in plastocyanin has 38% sulfur character (Section 4). Hence the pre-edge intensity of plastocyanin serves as a reference to calculate the transition dipole integral for thiolate. The value obtained is 8.05 (note that this corresponds to 0.027 normalized pre-edge intensity units per 1% thiolate-metal bond covalency in Eq. (8)), which is used to quantify covalency of other transition metal–thiolate bonds. The results for $Ni(II)(SR)_4$ indicate that, compared to 38% covalency of the Cu–S bond in plastocyanin, it has 17% sulfur character per Ni–S bond summed over two holes. The Ni–S bond is more covalent than the corresponding metal-chloride bond (5%) in spite of having one less π donor orbital (i.e. one S 3p orbital is involved in the S–C bond). The increase is due to increased σ covalency of thiolates along with better π overlap of the more extended sulfur orbitals.

5.1.2. Rubredoxin model complexes

The S K-edge XAS of two model complexes $[Fe^{III}(SPh)_4]^-$ and $[Fe^{III}(S_2\text{-}o\text{-xyl})_2]^-$ were reported [72] (Fig. 18). The XAS of the oxidized models have a well resolved pre-edge; the pre-edge of the reduced model is partially overlapped by the rising edge. Using an effective S_4 site symmetry for $[Fe^{III}(S_2\text{-}o\text{-xyl})_2]^-$, its pre-edge was fit using four peaks to resolve the transitions to ^5A, ^5B, ^5B and ^5E d^{n+1} excited states corresponding to transitions to the half occupied metal d orbitals (Fig. 18 inset). These peaks correspond to

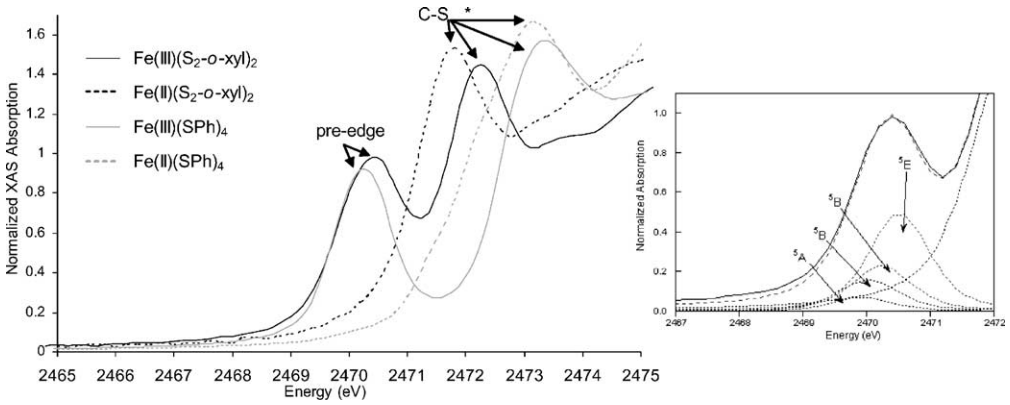

Fig. 18. S K-edge XAS spectra of rubredoxin model complexes $[Fe^{III/II}(S_2\text{-}o\text{-xyl})_2]^{-/2-}$ (black/dashed black) and $[Fe^{III/II}(SPh)_4]^{-/2-}$ (gray/dashed gray) The inset shows the pre-edge region of the $[Fe^{III}(S_2\text{-}o\text{-xyl})_2]^-$ S K-edge spectrum and includes a representative four-peak fit performed based on the d-orbital splitting diagram of Gebhard et. al. [73] with a 20% reduction in the splitting based on the effects of a core hole in the d-manifold in XAS. In inset the labelled peaks represent π contributions and the σ contributions. Each of the four peaks in the fit is labeled as the d^{n+1} parent state. The fit from the four peaks in the inset is given by the dashed line, while the data are represented by the solid line.

Table 9
Experimental edge energies (eV), intensities and covalencies of $[Fe(III)(SPh)_4]^-$ and $[Fe(III)(S_2\text{-}o\text{-}xyl)_2]^-$

	D_0[a]	Pre-edge position[b]	Rising edge inflection point[c]	Covalency per Fe–S bond (%)
$[Fe(III)(S_2\text{-}o\text{-}xyl)_2]^-$	1.15	2470.4	2472.2	38
$[Fe(III)(SPh)_4]^-$	1.03	2470.2	2472.6	32

[a] The total integrated pre-edge intensity from the normalized spectrum.
[b] Determined from the first minimum in the second derivative.
[c] Determined from the second minimum in the second derivative of spectra, which represents the sulfur 1s → C–S σ* transition.

one-electron transitions to the low symmetry (S_4) split e(π) $^5A + {}^5B$ (in Fig. 18 inset) and $t_2(\sigma)$ $^5B + {}^5E$ (in Fig. 18 inset) orbitals. The peak splittings were fixed using an energy diagram determined from other spectroscopic techniques [73]. The splittings were reduced by 20% to account for the fact that the final state has a reduced d^6 configuration. The fit gives a total hole covalency of 170% [72] (referenced to 38% S 3p character in the plastocyanin LUMO) which corresponds to sum of thiolate S π and pseudo σ[2] contributions to the four excited states from four thiolates, which is ∼38 % per Fe–S bond. The maximum π covalency was estimated to be 30% of the total observed covalency, which is consistent with the weak π and strong σ charge transfer transitions observed for this complex [73]. Spectroscopically calibrated SCF-Xα-SW calculations [72] gave 140% total covalency in reasonable agreement with experiment. However, the calculation gave a relatively higher estimate of π covalency.

Correlations between the two models show an interesting difference (Table 9). Based on the pK_a values of aromatic and aliphatic thiols (PhSH = 6.43 and EtSH = 10.61) one would expect a more nucleophilic ligand (higher pK_a) to have a higher 1s orbital energy and hence lower energy pre-edge and rising edge features. The C–S σ* transition energy of $Fe(III)(S_2\text{-}o\text{-}xyl)_2$ is lower than that of $Fe(III)(SPh)_4$; however the pre-edge follows the reverse order (1s → C–S σ* in Fig. 18). This can be explained by stronger charge donation (more covalent interaction) from the S_2-*o*-xyl ligand to Fe(III) increasing the Z_{eff} for the sulfur, decreasing Z_{eff} for Fe (shifting the pre-edge to high energy) and weakening the C–S bond, shifting the C–S σ* antibonding orbital to lower energy. This is also reflected in shorter Fe–S bond (2.27 Å) and longer C–S bond (1.86 Å) in $Fe(III)(S_2\text{-}o\text{-}xyl)_2$ as compared to $Fe(III)(SPh)_4$ (Fe–S = 2.30 and C–S = 1.78 Å) [74].

5.2. Binuclear Fe_2S_2 models of plant ferredoxins

Fe_2S_2 active sites are found in plant ferredoxins where two irons are bridged by two μ_2 sulfide bridges and each iron is ligated by two terminal cysteines or histidines in ferredoxins and Rieske proteins, respectively (Fig. 16c). These proteins perform one-electron transfer and their redox potentials vary from −400 to −200 mV in plant ferredoxins to + 280 to +180 mV in Rieske proteins [75]. The electronic structure of the active site has been well studied using different spectroscopic techniques [76–80] and is known to have two high spin anti-ferromagnetically coupled Fe(III) ions to give a diamagnetic ground state in its oxidized form. The reduced state, Fe(III)Fe(II), has a valence localized S = 1/2 ground state. However, there have been recent reports of a reduced valence delocalized ground state in a few mutants of *Clostridium pasteurianum* [82–84].

The S K-edge XAS of a representative $[Fe_2S_2(SR)_4]^{2-}$ model complex shows two distinct pre-edge features at 2469.6 and 2470.6 eV (Fig. 19a and b). The lowest energy feature at 2469.6 eV was assigned as the μ_2-sulfide 1s → metal d antibonding transition, while the higher energy feature at 2470.6 eV was assigned to a thiolate sulfur 1s → metal d antibonding transition. The lower energy of the sulfide peak reflects its 1s orbital energy which is higher relative to that of thiolate due to its higher electron density.

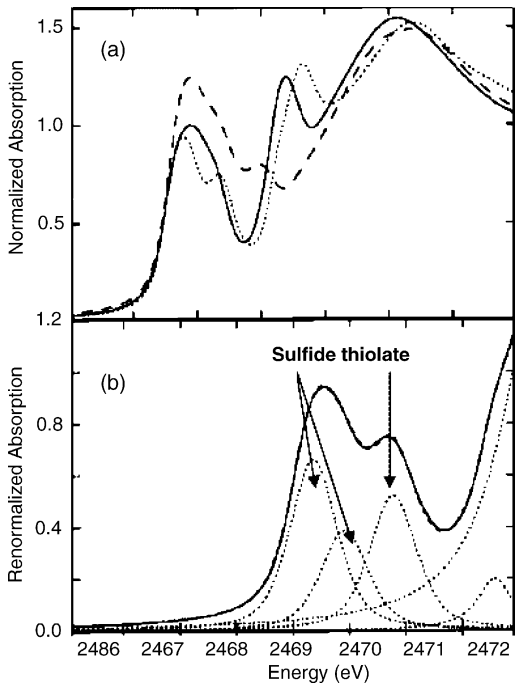

Fig. 19. (a) S K-edge XAS spectra of the fully oxidized Fe_2S_2 model complexes: $[Fe_2S_2(SEt)_4]^{2-}$ (—), $[Fe_2S_2(S_2\text{-}o\text{-}xyl)_2]^{2-}$ (- - -), and $[Fe_2S_2(SPh)_4]^{2-}$ (···). (b) Representative fit to the pre-edge region of the S K-edge XAS spectrum of $[Fe_2S_2(SPh)_4]^{2-}$.

[2] Note that as with blue copper in Section 4.1 the σ bond is referred to as pseudo σ as it is tilted off the bond axis when the Fe-S-C angle is >90°.

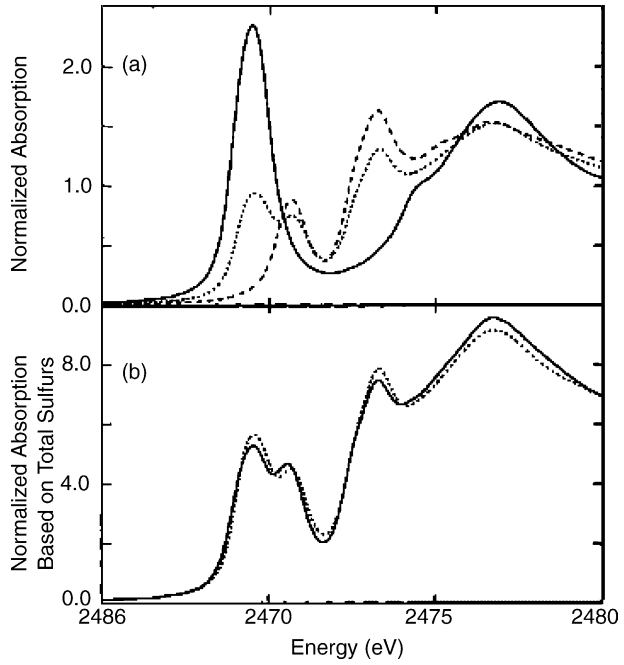

Fig. 20. (a) Normalized S K-edge XAS spectra of $[Fe_2S_2Cl_4]^{2-}$ (—), $[Fe_2Se_2(SPh)_4]^{2-}$ (---) and $[Fe_2S_2(SPh)_4]^{2-}$ (···); (b) Normalized S K-edge XAS spectra of $[Fe_2S_2(SPh)_4]^{2-}$ (···) and normalized summation of $[Fe_2S_2Cl_4]^{2-}$ and $[Fe_2Se_2(SPh)_4]^{2-}$ (—).

This was confirmed experimentally [85] from the S K-edge XAS of thiolate-substituted and sulfide-substituted model complexes $[Fe_2S_2Cl_4]^{2-}$ and $[Fe_2Se_2(SPh)_4]^{2-}$ (Fig. 20a). The sum of these two spectra reproduce the spectrum of $[Fe_2S_2(SPh)_4]^{2-}$ quite well after renormalization, confirming the assignments (Fig. 20b).

To understand the Fe–$S_{sulfide}$ bonding, a standard, relating the pre-edge intensity to percentage covalency was needed. The covalency of $KFeS_2$, an infinite chain of bis-(μ-sulfido) bridged ferric ions, was estimated from XPS to be 42% sulfide per iron orbital [85,86]. Assuming this to be the same for the isomorphous $CsFeS_2$ complex, its pre-edge intensity was used as a reference. The transition dipole integral of the μ_2 sulfide was estimated to be 6.54 (this corresponds to 0.046 normalized pre-edge intensity per 1% sulfide–iron bond covalency in Eq. (8), 18% lower than that of thiolate (8.05 vide supra). This is due to increased negative charge density on sulfide which increases the radial distribution of sulfur 3p orbital and decreases the overlap with the 1s orbital lowering the transition probability.

The results of the fits to the pre-edge for the Fe_2S_2 model complexes are shown in Table 10. The sulfide covalency decreases from $[Fe_2S_2Cl_4]^{2-}$ to $CsFeS_2$. Also the thiolate covalency is reduced to 25% per Fe–$S_{thiolate}$ bond in $Fe_2S_2(SEt_4)$ complexes from the 35% in the equivalent iron tetrathiolate monomers (Table 9). Both reductions suggest that the μ_2-sulfide is the major electron donor to the irons in $Fe_2S_2(SR)_4$ clusters. This can be due to increased σ covalency in the sulfide and/or the increased e(π) donation [87].

S K-edge data of the various Fe_2S_2 complexes show variations in both the intensity and the energy of transitions. A significant difference is observed when comparing the spectra of $[Fe_2S_2(SPh)_4]^{2-}$ and $[Fe_2S_2(S_2\text{-}o\text{-xyl})_2]^{2-}$ (Fig. 19). The pre-edge feature assigned to the thiolate (peak at 2470.6 eV in Fig. 19) in $[Fe_2S_2(SPh)_4]^{2-}$ shifts to lower energy in $[Fe_2S_2(S_2\text{-}o\text{-xyl})_2]^{2-}$. This is contrary to our observation in the iron tetrathiolate case where the stronger charge donation from the ligand with the higher pK_a (S_2-*o*-xyl) results in its shift to higher energy. However, for the Fe_2S_2 centers, the μ_2-sulfides are the major donors; thus the charge transfer from the thiolate ligands to the Fe is significantly decreased, and accordingly the ligand having the higher pK_a has higher negative charge and a 1s orbital higher in energy resulting in a lower energy pre-edge transition.

A correlation was made between the total ligand character and the redox potentials of a series of Fe_2S_2 model complexes [88]. The total ligand covalencies of the $[Fe_2S_2(S_2\text{-}o\text{-xyl})_2]^{2-}$, $[Fe_2S_2(SEt)_4]^{2-}$, $[Fe_2S_2(SPh)_4]^{2-}$, and $[Fe_2S_2Cl_4]^{2-}$ are 266, 206, 204, and 156%, respectively. Their corresponding reduction potentials are −1.49, −1.31, −1.09 and −0.82 mV [89–91] versus SCE, respectively. As observed in Fig. 21 there is a direct correlation between total covalency and E^0, which reflects the fact that the better donor ligands stabilize the oxidized state more than the reduced state to lower the reduction potential. Compared to the total hole orbital covalency of the tetrathiolates (170%), the total orbital covalency of the $Fe_2S_2(SR)_4$ dimers is higher (200–300%) due to the strong charge donation from the sulfide ligands.

Table 10
Experimental pre-edge intensity and covalency of Fe_2S_2 model complexes

Compound	Sulfide intensity	Covalency of one sulfide per iron (%)	Thiolate intensity	Covalency of one thiolate per iron (%)
$Fe_2S_2(SPh)_4^{2-}$	3.15	72	0.80	30
$Fe_2S_2(S_2\text{-}o\text{-xyl})_2^{2-}$	4.38	100	0.87	33
$Fe_2S_2(SEt)_4^{2-}$	3.39	78	0.67	25
$Fe_2Se_2(SPh)_4^{2-}$			0.84	31
$Fe_2S_2Cl_4^{2-}$	2.84	65	0.94	13[a]
$CsFeS_2$	2.42	52		

[a] Terminal chloride covalency.

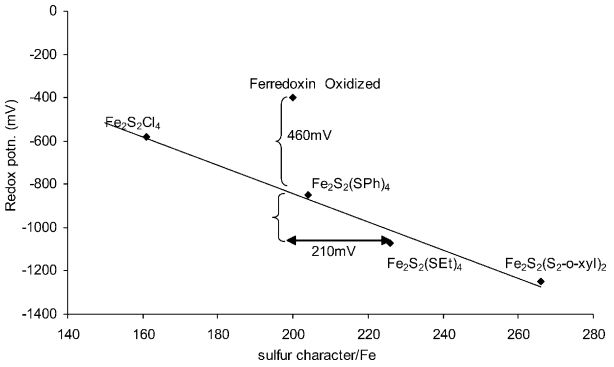

Fig. 21. Plot of total ligand character per iron measured from ligand K-edge XAS of Fe_2S_2 model complexes vs. redox potential. A linear correlation is obtained. For the protein active site (Section 5.5.2) the decrease in covalency due to H-bond contributes to about 1/3 of the observed deviation from the closest model complex. The rest 2/3 is protein effect.

5.3. Fe_4S_4 models of bacterial ferredoxins and high potential iron–sulfur proteins (HiPIPs)

These are the major electron transport proteins in bacteria and higher organisms. Their active sites have an Fe_4S_4 cubic core with μ_3 sulfide atoms occupying alternate corners of the cube and cysteine residues from the backbone coordinating to each iron atom (Fig. 16e). These proteins can be divided into two classes based on their redox behavior: ferredoxins involve the lower redox couple $[Fe_4S_4]^{2+} \leftrightarrow [Fe_4S_4]^{1+}$ ($E_0 = -250$ to -450 mV) whereas HiPIPs involve the higher redox couple $[Fe_4S_4]^{3+} \leftrightarrow [Fe_4S_4]^{2+}$ ($E_0 = 300$ to 600 mV). The intermediate $[Fe_4S_4]^{2+}$ state is described as two valence-delocalized, ferromagnetically coupled, $S = 9/2$ $[Fe_2S_2]^{+}$ units anti-ferromagnetically coupled to give a diamagnetic $S = 0$ ground state. The oxidized cluster has an $S = 1/2$ ground state and the reduced cluster exists as a mixture of $S = 1/2$, 3/2 and higher spin states [92].

5.3.1. Bonding in model complexes

Sulfur K-edge XAS of the Fe_4S_4 model complex $[Fe_4S_4(SPh)_4]^{2-}$ and related clusters are shown in Fig. 22a. The spectrum of $[Fe_4S_4(SPh)_4]^{2-}$ is dominated by a large broad pre-edge transition at 2470 eV and a 1s → C–S σ* transition at 2472 eV. The second derivative of the spectrum (Fig. 22b) shows the presence of two features in the envelope of the pre-edge transition. The resolution of the peaks is not as high as in the case of $Fe_2S_2(SR)_4$ cluster in Fig. 20, as the μ_3-sulfide transition has shifted to a higher energy compared to the μ_2-sulfide in Fe_2S_2 (Fig. 22a) by about 0.6 eV, decreasing its peak separation from the thiolate pre-edge feature at 2471.0 eV. The shift of the sulfide pre-edge position to a higher energy is a result of the reduced charge density on a μ_3-sulfide compared to a μ_2-sulfide and the shift of the iron orbitals up in energy as the formal oxidation state of the irons decreases from 3 to 2.5 in the $[Fe_4S_4]^{2+}$ clusters.

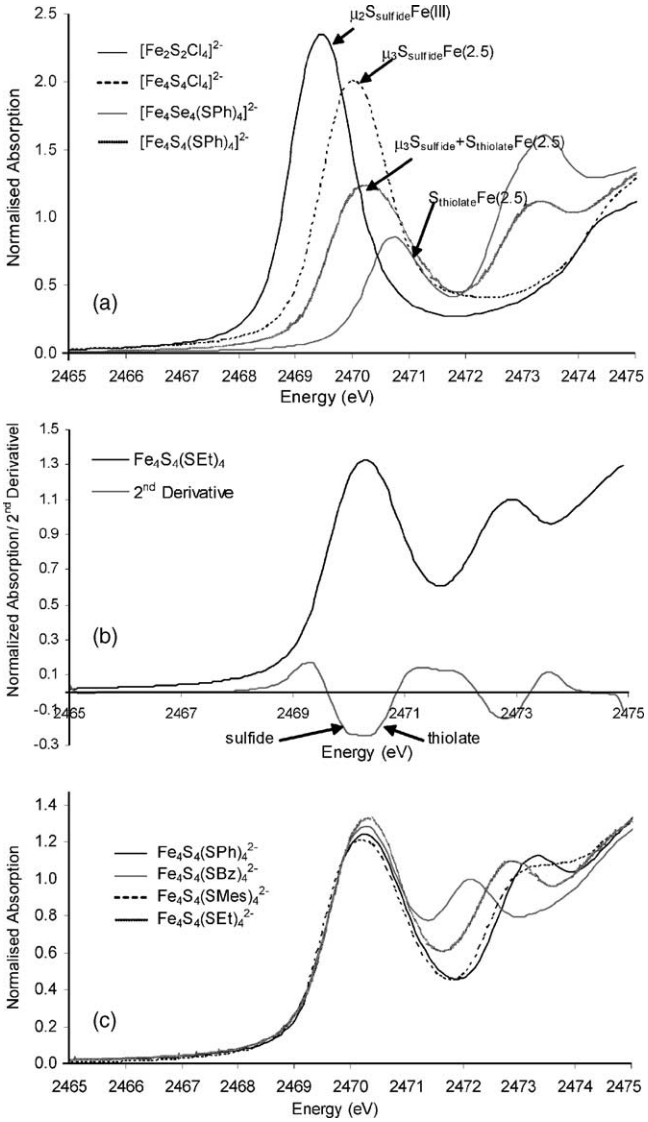

Fig. 22. (a) S K-edge XAS spectra of $[Fe_2S_2Cl_4]^{2-}$ (—), $[Fe_4S_4(SPh)_4]^{2-}$ (. . .), $[Fe_4S_4Cl_4]^{2-}$ (- - -), and $[Fe_4Se_4(SPh)_4]^{2-}$ (· · ·). (b) S K-edge XAS spectra $[Fe_4S_4(SPh)_4]^{2-}$ and its second derivative showing the presence of two features under one envelope. (c) S K-edge XAS spectra of $[Fe_4S_4(SR)_4]^{2-}$ models where R= SPh (—), SBz (· · ·), SMes (¯ ¯), and SEt (- - -).

However the relative energy ordering of the sulfide and thiolate features remains the same as evident from the spectra of the thiolate-substituted and sulfide-substituted clusters $[Fe_4S_4Cl_4]^{2-}$ and $[Fe_4Se_4(SPh)_4]^{2-}$ [93] (Fig. 22a). The S K-edge XAS of $[Fe_4S_4(SBz)_4]^{2-}$, $[Fe_4S_4(SEt)_4]^{2-}$, and $[Fe_4S_4(SMes)_4]^{2-}$ [95,96] show similar features (Fig. 22c). As for the Fe_2S_2 clusters, the 1s → C–S σ* transitions in these complexes follow the trend expected from their nucleophilicity, i.e. the aromatic thiolates have their 1s orbitals at deeper binding energies than the aliphatic thiols. This indicates that, like for the binuclear clusters, the sulfides are the major electron donors to the irons in the Fe_4S_4 clusters.

To quantify the bonding of a μ_3-sulfide, a standard for the transition dipole moment integral (D_0) was needed. Ex-

Table 11
Experimental pre-edge intensities and covalencies of Fe_4S_4 and related Fe_2S_2 model complexes.

	μ_3/μ_2 Sulfide			Thiolate/chloride		
	D_0[a]	Position	Covalency[b]	D_0[a]	Position	Covalency[b]
$Fe_2S_2Cl_4^{2-}$	2.96 ± 0.1	2469.5	68 ± 2	1.07 ± 0.1	2821.6	15 ± 1
$Fe_2S_2(SEt)_4^{2-}$	1.13 ± 0.05	2469.6	78 ± 3	0.45 ± 0.05	2470.6	25 ± 3
$Fe_4S_4Cl_4^{2-}$	2.5 ± 0.18	2470.1	39 ± 3	1.03 ± 0.1	2821.8	15 ± 1
$Fe_4S_4(SEt)_4^{2-}$	1.72 ± 0.05	2470.1	41 ± 2	0.7 ± 0.05	2470.9	41 ± 2

[a] D_0 is the normalized pre-edge intensity of individual components.
[b] Covalency is expressed as % covalency per metal ligand bond.

perimentally the 1s → 4p transition for $[Fe_2S_2Cl_4]^{2-}$ and $[Fe_4S_4Cl_4]^{2-}$ are at similar energy (Fig. 22a). Based on the fact that the μ_3-sulfide is ligated to three Fe(2.5) centers one might expect its 1s orbital to be at deeper binding energy than a μ_2-sulfide which is ligated to two Fe(III) centers. However the μ_2-sulfides donate more charge to Fe(III) than the μ_3-sulfide does to Fe(2.5), which results in similar 1s → 4p transition energies and Z_{eff} for both μ_3- and μ_2-sulfides. Hence the D_0 will not change significantly between the two kinds of bridging sulfide ligands. Therefore the value obtained for $KFeS_2$ (6.54) was used to quantify the Fe–$S_{sulfide}$ bonding in Fe_4S_4 clusters. The results of the fits to the experimental spectra (Table 11) show that the μ_3-sulfide–iron bond (note that this is a per bond estimate) has a covalency of ∼39% in $[Fe_4S_4Cl_4]^{2-}$ as compared to the 65% covalency of the μ_2-sulfide–iron bond in $[Fe_2S_2Cl_4]^{2-}$. Since the μ_3-sulfide donates charge to three Fe(2.5) centers, the individual Fe–$S_{sulfide}$ bond covalency is less than for the μ_2-sulfide, which donates charge to only two Fe(III) centers. In addition, the iron thiolate bond covalency increases from 25% in $[Fe_2S_2(SEt)_4]^{2-}$ to 35% in $[Fe_4S_4(SEt)_4]^{2-}$. This shows that the thiolates behave as spectator ligands which adjust the extent of charge transfer to the iron in response to the change in charge transfer from the bridging sulfides, which are the stronger donor ligands.

5.3.2. Oxidized and reduced [Fe_4S_4] clusters

The ligand K-edge methodology has recently been extended to oxidized and reduced $[Fe_4S_4]$ clusters. The clusters show large changes in total hole covalency when they are reduced (Fig. 23a) or oxidized (b) from the resting $[Fe_4S_4]^{2+}$ state. The model complexes $[Fe_4S_4(SEt)_4]^{2-}$ and $[Fe_4S_4(SMe)_4]^{3-}$, representing the ferredoxin couple, have total ligand character per hole as 37 and 35%, respectively. The HiPiP oxidized and reduced proteins (note that the HiPiP reduced has a very similar pre-edge intensity to the $[Fe_4S_4(SEt)_4]^{2-}$ model complex) have total ligand character per hole as 37 and 32%, respectively. Thus in both redox couples the covalency per hole changes and the change is more than twice in the HiPiP couple than the ferredoxin couple (redox difference plot in Fig. 23c). These interesting observations relate to the nature of the redox active molecular orbital (RAMO) and electronic relaxation involved in

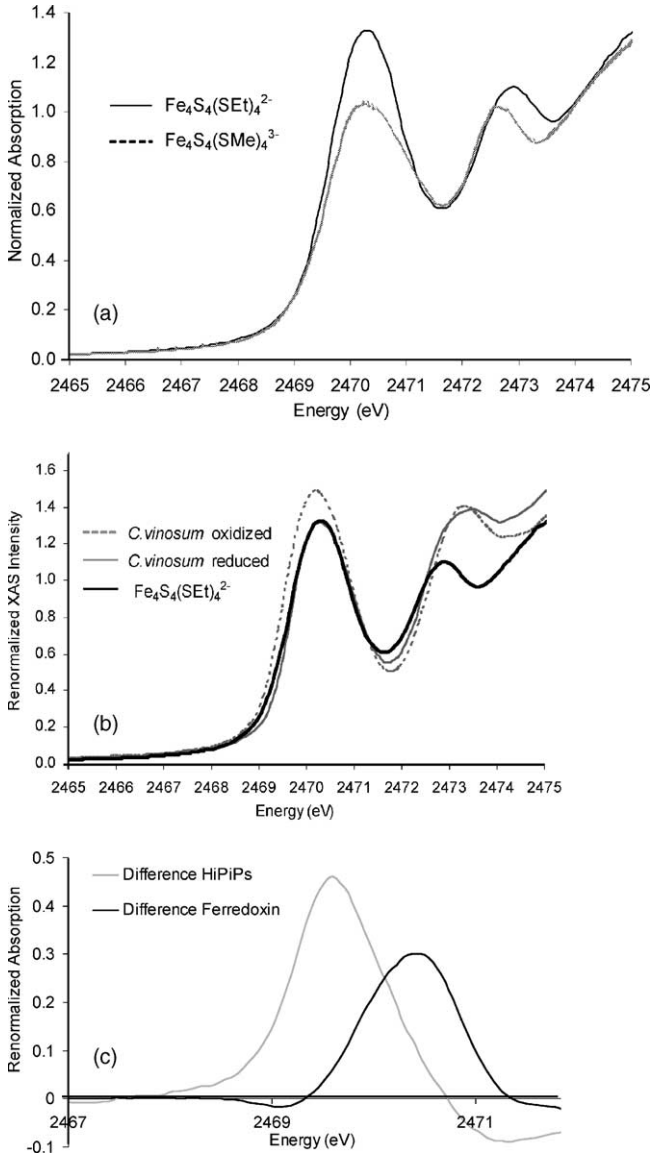

Fig. 23. (a) S K-edge XAS spectra of $[Fe_4S_4(SEt)_4]^{2-}$ (black) and $[Fe_4S_4(SMe)_4]^{3-}$ (dotted). (b) S K-edge XAS of HiPiP in its oxidized state $[Fe_4S_4]^{3+}$(dotted grey) and resting form $[Fe_4S_4]^{2+}$ (grey) and the model complex $[Fe_4S_4(SEt)_4]^{2-}$ (black). (c) Difference S K-edge XAS spectrum of Fd (black) and HiPiP (grey) redox couples.

the redox process of these clusters which are currently under investigation [94].

5.4. Fe_3S_4 models of ferredoxin II proteins

The Fe_3S_4 active site has been identified as a functional unit in a number of enzymes e.g ferredoxin II from *Desulfovibrio gigas*, *Azotobacter vinelandii*, etc. Although its function in some cases remains to be determined, for several enzymes it is known to be involved in electron transport [97,98]. The cuboidal structure of an Fe_3S_4 active site (Fig. 16d) can be viewed as resulting from removal of one Fe and its terminal cysteine ligand from an Fe_4S_4 cube. This produces both μ_2-and μ_3-sulfides. In its resting $[Fe_3S_4]^0$ form, the cluster contains a valence-delocalized S = 9/2 $[Fe_2S_2]^{1+}$ unit anti-ferromagnetically coupled with a high spin Fe(III) to give an S = 2 ground state [99–102]. When oxidized, the cluster has all high spin Fe(III) ions coupled to give a spin frustrated S = 1/2 ground spin state [100,101]. S K-edge spectra of Fe_3S_4 clusters in ferredoxin II from *D. gigas* and its model complex have recently been measured [103].

5.4.1. Bonding in the Fe_3S_4 cluster

The S K-edge XAS of a Fe_3S_4 model complex (Fig. 24a) and its selenide-substituted analogue show the thiolate to be the highest-energy feature at 2471.0 eV. The two types of bridging sulfides contribute to the broad envelope of transitions at lower energy (between 2469.0 and 2470.6 eV). Based on previous S K-edge XAS results the μ_2-sulfide contribution should be at a lower energy than the μ_3-sulfide (Fig. 24b). From fits to the experimental data, the total μ_2-, μ_3-sulfide and the thiolate hole covalencies were obtained. Initial results indicate that the μ_2-sulfide bond in the delocalized $[Fe_2S_2]^+$ cluster of the $[Fe_3S_4]^0$ is less covalent (46%) than μ_2-sulfide bond in the reduced Fe_2S_2 cluster (61%) due to strong charge transfer from the additional μ_2-sulfides bridging the Fe(2.5) to the Fe(III) center (Fig. 16d). The μ_3-sulfide iron bond in the Fe_2S_2 delocalized cluster was estimated to have 30% covalency, 9% less than the μ_3-sulfide iron bond in $[Fe_4S_4]^{2+}$, which was 39%. This is due to the additional coordination of the μ_3-sulfide to Fe(III) which is a stronger charge acceptor than Fe(2.5), along with strong charge donation by the μ_2-sulfides to the Fe(2.5).

In summary, the bridging sulfide covalency of the Fe_2S_2 sub-cluster of the resting $[Fe_3S_4]^0$ cluster decreases from expected values (based on the bridging ligand covalency of the Fe_2S_2 and Fe_4S_4 clusters) mainly due to the stronger donation by additional μ_2-sulfides (Fig. 16d) and the presence of the Fe(III).

5.4.2. Redox changes in $[Fe_3S_4]$ clusters

The S K-edge XAS of oxidized and reduced protein ferredoxin II from *D. gigas* (Fig. 25) shows a large increase in total hole covalency on oxidation. The increase is more than statistical (i.e. increase in the number of holes) as the total ligand character per hole increases from 22% in the reduced form to 30.5% in the oxidized form. Interestingly the charge donations from the sulfides and thiolates increase by different amounts. This reflects different involvement of these ligands in the redox process and is currently under investigation [103].

5.5. Protein effects in iron–sulfur clusters: effect of H-bonding on Fe–S covalency

Other than their different structural motifs, iron–sulfur proteins differ significantly in their redox potentials. The

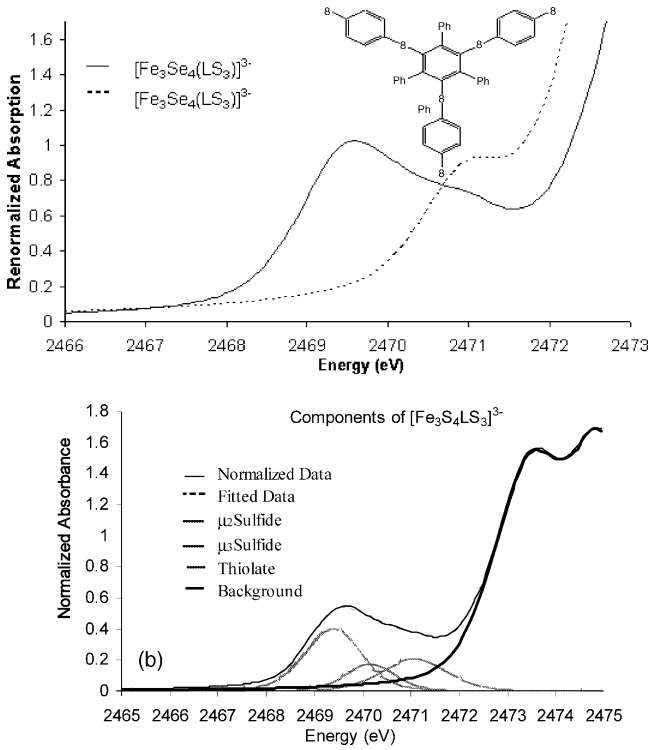

Fig. 24. (a) S K-edge XAS spectra of Fe_3S_4 model complexes $[Fe_3S_4(LS_3)]^{3-}$ (—) and $[Fe_3Se_4(LS_3)]^{3-}$ (- - -). (b) Normalized S K-edge XAS spectrum of $[Fe_3S_4(LS_3)]^{3-}$ (—) the fitted spectrum (- - -) and showing the presence of three features (···) in the pre-edge region μ_2-sulfide, μ_3-sulfide, thiolate and background (–).

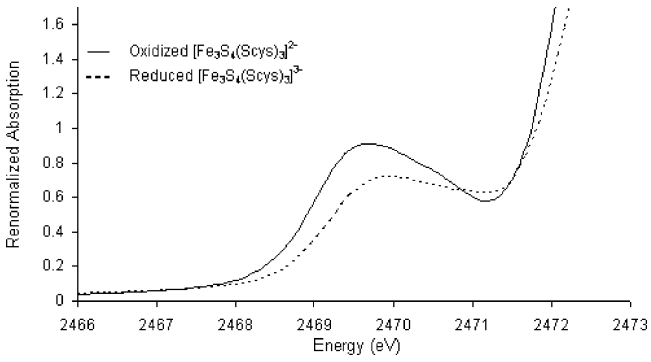

Fig. 25. S K-edge XAS spectra of oxidized (—) and reduced (- - -) ferredoxin II from *D. gigas*.

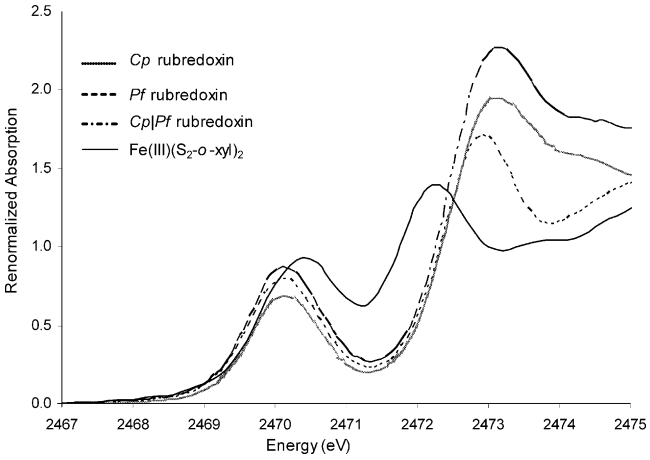

Fig. 26. S K-edge XAS spectra of Oxidized Rubredoxin proteins Cp (···), Pf (- - -), Cp/Pf (-.-.-), and the model $[Fe^{III}(S_2\text{-}o\text{-xyl})_2]^-$ (—).

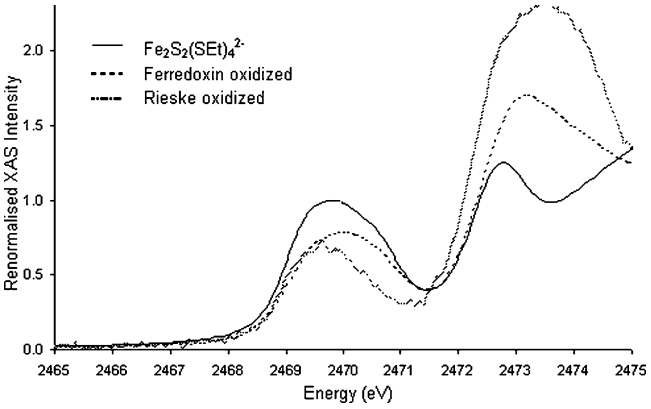

Fig. 27. S K-edge XAS spectra of Rieske protein (···), spinach ferredoxin (- - -) and a model complex $Fe_2S_2(SEt)_4^{2-}$ (—).

difference in the redox potential between proteins from different organisms having the same active site structure can be as much as 1 V [104]. In contrast, model complexes having a similar structure have quite similar redox potentials. Hence it is important to understand the effects that contribute to the redox potential of a protein active site. In addition to protein dielectric effects, solvent accessibility, H-bonds and surrounding peptide dipoles can make significant contributions to the redox potentials based on experimental [105–109] and computational results [110,111]. S K-edge XAS has proved to be a powerful probe of H-bonding to sulfur ligands as this method directly probes the covalency of the Fe–S bond.

The amount of charge transfer from the ligands to the metal, i.e. covalency of the M–L bond, makes a very significant contribution to the redox potentials particularly in covalent systems like the iron–sulfur proteins. Increased covalency stabilizes the higher oxidation state reducing the reduction potential of the system. In the presence of H-bonds to the sulfur, the charge transfer of the ligand to the metal should decrease and the redox potential should become more positive.

5.5.1. Rubredoxins

The S K-edge XAS spectra of rubredoxins from three different organisms, *C. pasteurianum* (Cp), *Pyrococcus furiosus* (Pf) and a mutant having half the sequence from each of the above two proteins (Cp/Pf), are shown in Fig. 26 along with data of the model complex $[Fe(S_2\text{-}o\text{-xyl})_2]^-$ [72]. The proteins display an intense pre-edge feature at approximately the same energy as for the model complex.

The intensity of the transition is lower than that of the model complex; however, and this reduction varies in magnitude for the different proteins. This reduction in pre-edge intensity implies a reduction in Fe–$S_{thiolate}$ bond covalency, which was quantified by fits to the experimental spectra (Table 12). The total hole covalency for the four thiolate-Fe(III) bonds is 125–130% in the proteins compared to 170% in the model. The protein active sites have 6 backbone N–H–S(Cys) H-bonds reducing the covalency of these sites. The redox potentials of these proteins are ∼1 V higher than for for the model complex. This is partly due to the H-bonds to the site and partly due to other protein effects. These effects could be separately estimated for the Fe_2S_2 clusters as discussed below.

5.5.2. Fe_2S_2 clusters in ferredoxins and Rieske proteins

S K-edge XAS of spinach ferredoxin and a Rieske protein are shown in Fig. 27 together with the S K-edge XAS data for the model system $[Fe_2S_2(SEt)_4]^{2-}$ [85,88]. The proteins have similarly broad pre-edge features but are much less intense than the pre-edge feature of the model complex. Since there are two contributions to the pre-edge, from sulfide and thiolate, fits were performed to quantify the decrease in covalency for each type of ligand (Table 13). The intensities, renormalized to total number of sulfur absorbers contributing to the pre-edge, show that the covalency of the thiolates

Table 12
Results of the pre-edge fits for rubredoxin proteins and models

Sample	Normalized pre-edge intensity	Renormalized pre-edge intensity[a]	Rescaled total S covalency[b] (%)
$[Et_4N][Fe(o\text{-}C_6H_4(CH_2S)_2)_2]$	1.15	1.15	171 ± 3
CfRd	0.96	0.96	125 ± 6
PfRd	0.83	1.03	135 ± 8
Cp15|*Pf*Rd	0.79	0.98	129 ± 7

[a] The observed intensity has to be scaled up to account for the extra methionine and cysteine sulfurs in the protein that contributes to the edge-jump but does not contribute to the pre-edge.
[b] The covalency reported here is total % thiolate character after renormalization.

Table 13
Experimental intensities and covalencies from S K-edge XAS of oxidized and reduced Rieske, ferredoxin proteins and oxidized model $[Fe_2S_2(SEt)_4]^{2-}$

	Sulfide			Thiolate		Total Ligand character[b]
	D_0		Covalency[a]	D_0	Covalency[a]	
Ferredoxin oxidized	0.96		77	0.36	23	200
Ferredoxin	Fe(III)	0.51	82	0.19	25	na
Reduced	Fe(II)	0.14	33	nr	nr	
Rieske oxidized	0.77		71	0.23	34	198
Rieske reduced	Fe(III)	0.36	67	0.22	32	na
	Fe(II)	nr	nr	nr	nr	
$Fe_2S_2(Set)_4^{2-}$	1.29		88	0.42	25	225

[a] Covalency is reported as percentage per metal–ligand bond.
[b] Total ligand character is per iron(nr implies not resolved; na implies not applicable).

remain essentially the same between the oxidized ferredoxin protein and the model complex (23% versus 25%) despite the fact that there are H-bonds to the thiolates in the proteins. However the iron sulfide bond covalency decreases from 88% in the model to 77% in spinach ferredoxin and 71% in the oxidized Rieske protein. Such a trend correlates very well with the presence of three H-bonds to the sulfides in spinach ferredoxin and four in the Rieske protein. Sulfides, having more negative charge density, are affected more by the H-bonds than the thiolates. The redox potentials qualitatively follow the trend expected from the observed change in covalency, −1.31 V for the model [90], −400 mV for spinach ferredoxin [88] and +280 mV for Rieske [85]. The large difference between the redox potentials of spinach ferredoxin and the Rieske protein is mostly due to the fact that the Rieske center has two histidine ligands to one Fe (Fig. 16c), which are poorer donors than thiolates, and this results in an increase of the potential for the iron to which they coordinate. Including the oxidized ferredoxin protein value in the correlation diagram relating redox potential and covalency (Fig. 21) established that the effect of H-bonding accounts for about 1/3 of the difference of the redox potential between the spinach ferredoxin and its model complex (with aliphatic thiolate), while 2/3 is due to other protein environment effects (dielectric, etc.).

Upon reduction (Fig. 28) both protein centers lose pre-edge intensity. In the absence of a reduced model complex, the effect on the protein covalency could not be quantified, though it can be expected that the effect of H-bonding will be higher in the reduced state where there is more negative charge density. The proteins, however, offered the opportunity to study the S K-edge XAS spectra of a localized Fe_2S_2 reduced site, which is not presently available in models as reduced Fe_2S_2 clusters dimerize to form Fe_4S_4 clusters. As expected from the S K-edge of mono-nuclear Fe(II) thiolate complexes, the Fe(II)-$S_{thiolate}$ pre-edge overlaps with the intense rising-edge feature at ~2472 eV. However, the Fe(II)-$S_{sulfide}$ feature was observed at 2470.8 eV and could be quantified for spinach ferredoxin (Table 13). It was found to have 33% covalency, much less than that of Fe(III)-$S_{sulfide}$ (82%). Since the nuclear charge of iron is reduced and there is one fewer π hole, such a decrease is expected. In parallel the charge transfer to the Fe(III) center in the reduced ferredoxin (82%) increased from 77% in the oxidized protein. The Rieske protein in its reduced form showed no decrease in its thiolate feature (i.e. the thiolate coordinated Fe in Fig. 16c is not the one reduced) although the sulfide contribution decreased in its pre-edge transitions. Quantitative fits to the spectra showed that the pre-edge intensity of the Fe(III)-bound thiolate did not change, indicating that the thiolates are insensitive to the reduction of the second iron site.

5.5.3. Fe_4S_4 clusters in bacterial ferredoxins and HiPIPs

The effects of the protein matrix on the redox properties of the Fe_4S_4 cluster have been intensely studied. It is important to understand why different redox couples are operational for the Fe_4S_4 clusters in HiPIPs ($[Fe_4S_4]^{3+/2+}$) and ferredoxins ($[Fe_4S_4]^{2+/+}$) (Section 5.3). S K-edges have been used to estimate the protein effect on Fe–S bond covalency in these Fe_4S_4-cluster containing proteins (Fig. 29). From high-resolution X-ray crystal structures its known that HiPIP has one H-bond to its μ_3 sulfides and four to the thiolates and that they are located in the hydrophobic core of the protein [112]. However, ferredoxins have three H-bonds to the sulfides and four to the thiolates, and the clusters are located

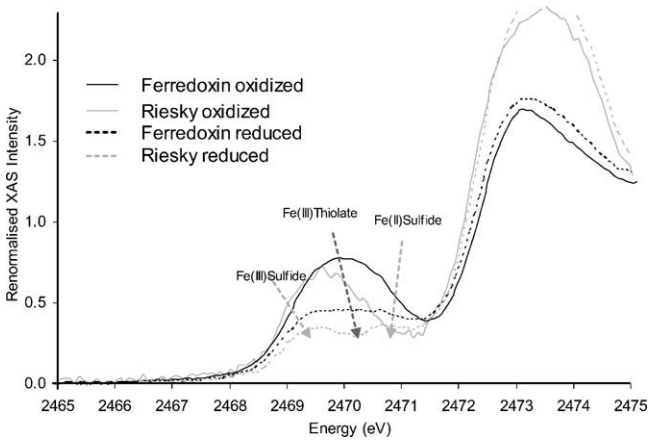

Fig. 28. S K-edge XAS spectra of reduced (- - -) and oxidized (—) Rieske (grey) and spinach ferredoxin (black) proteins.

Table 14
Experimental pre-edge intensity and covalencies of Fe_4S_4 proteins and related model complexes

	Sulfide			Thiolate		
	D_0	Energy	Covalency[a] (%)	D_0	Energy	Covalency[a] (%)
HiPiP	1.57	2470.1	37	0.69	2470.9	40
Ferredoxin	0.96	2469.9	23	0.51	2470.8	30
$Fe_2S_2(Set)_4^{2-}$	1.72	2470.1	41	0.7	2470.9	41

[a] Covalency per metal ligand bond.

close to the surface of the protein [113]. The S K-edge data of the proteins and the corresponding model in their resting form ($[Fe_4S_4]^{2+}$) (Fig. 29) show that there is very little difference in pre-edge intensity between the HiPIP protein and its model while the difference is large in ferredoxin [114]. From the fits to the data (Table 14) it was found that the sulfide intensity decreases by 18% per Fe–$S_{sulfide}$ bond in bacterial ferredoxin, while the Fe–$S_{sulfide}$ bond covalency decreases by only 1% in HiPIP. From the fits to the thiolate intensity, the change in Fe–$S_{thiolate}$ bond covalency is also quite insignificant for HiPIP, but is about 10% for ferredoxin. Such a significant difference between the covalency of the active sites of ferredoxin and HiPIP, in the same redox state ($[Fe_4S_4]^{2+}$), correlates well with the number of H-bonds to the active site ligands, and their location in the protein. The much larger charge transfer to the irons in the HiPIP active site can stabilize the higher oxidation state ($[Fe_4S_4]^{3+}$) leading to the high potential couple ($E_0 = 350$ mV) while the ferredoxins, having less charge density, utilize a +2/+1 couple leading to a low potential ($E_0 = -400$ mV).

5.6. Electronic delocalization in Fe_4S_4 clusters

Both $[Fe_4S_4]^{2+}$ and $[Fe_3S_4]^0$ clusters have a delocalized Fe_2S_2 binuclear unit anti-ferromagnetically coupled to another Fe_2S_2 delocalized unit or a high spin Fe(III) ion, respectively [98,115,116]. This delocalization is in contrast to the electronic structure of the reduced Fe_2S_2 centers, which is localized [78]. The delocalization of the excess electron in the mixed-valence state is accompanied by a net ferromagnetic coupling between the iron centers leading to an $S_t = 9/2$ dimer ground state. This phenomenon of spin alignment in mixed-valence systems with delocalized ground states is called double exchange in analogy to Kramer's superexchange mechanism [117,118]. The physical origin of double exchange elucidated by Girerd, Münck and coworkers, [81,99,119] and Noodleman and Baerends [80], is that electron transfer leads to a loss of spin polarization energy for the antiferromagnetic, but not for the ferromagnetic configuration.

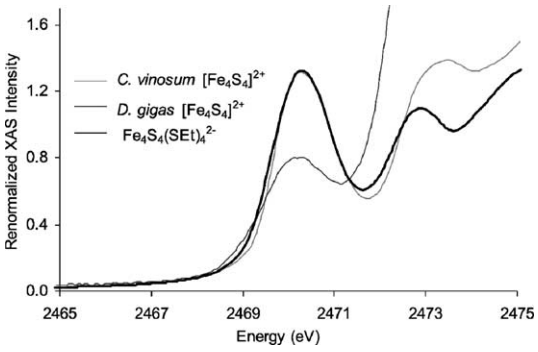

Fig. 29. S K-edge XAS spectra of *D. gigas* ferredoxin I (—) and *C. vinosum* HiPIP (···) and their model complex, $Fe_4S_4(SEt)_4^{2-}$ (—). The oxidation states are indicated by the total charge on the Fe_4S_4 cores.

There are three interactions to consider between the magnetic centers in a mixed-valence pair, namely superexchange (parameterized by J (using $H = -2J\mathbf{S}_1\mathbf{S}_2$)), double exchange ($B$), and vibronic coupling ($\lambda 2/k_-$). The energies of the spin states are given by:

$$E \pm (S_T) = -JS_T(S_T+1) + \frac{1}{2}\left(\frac{\Lambda^2}{k_-}\right)x_-^2 \pm \sqrt{\frac{1}{2}\left(\frac{\Lambda^2}{k_-}\right)^2 x_-^2 + B^2\left(S_T+\frac{1}{2}\right)^2} \quad (10)$$

Superexchange leads mainly to antiferromagnetic coupling, whereas double exchange leads to delocalization of the excess electron and to ferromagnetic coupling. Vibronic coupling is the driving force for localization of the excess electron. The interplay between these three interactions leads to interesting potential energy surfaces for the spin states in the antisymmetric breathing mode Q_-,[3] Double exchange, as the driving force for electron delocalization, is more effective in the higher spin states. Thus, strong superexchange, which leads to antiferromagnetic coupling and stabilization of the lower spin states, makes the double exchange less effective and thus decreases the tendency for electron delocalization. It had been thought that the delocalization of the excess electron in the mixed-valence $[Fe_2S_2]^+$ sub-dimers of $[Fe_3S_4]^0$ and $[Fe_4S_4]^{1+,2+,3+}$ originates from spin frustration. The spins in these clusters cannot all be aligned antiferromagnetically due to the presence of three or four approximately equal bridged spin centers. This reduces the effect of the antiferromagnetic coupling and increases the tendency toward delocalization through double exchange.

[3] The parameter x_- in Eq. 1 is the dimensionless coordinate associated with the Q_- vibrational normal coordinate (Q_-) having vibrational frequency ν_- and the force constant $k_- = 4\pi^2c^2m\nu^2$ for the nuclear distortion along this coordinate.

A relation between J and the experimentally observed bridging ligand covalency (from ligand K-edge XAS) has been derived using a Valence Bond Configuration Interaction (VBCI) model for superexchange, where LMCT states CI mix with the VB ground state [93].

$$J\alpha \text{ (covalency)}^2 \quad (11)$$

As discussed in earlier sections, the bonding in Fe_4S_4 clusters is quite different from that of the Fe_2S_2 cluster. A reduced Fe_2S_2 cluster is bridged by two very covalent μ_2 sulfides. According to Eq. (11), high bridging-ligand covalency increases the super exchange interaction and favors an antiferromagnetic ground state. However, in the Fe_4S_4 cluster, the bridging ligand is a μ_3 sulfide, which donates charge to three metal centers. As a result the average $Fe–S_{sulfide}$ covalency is lowered in the Fe_4S_4 cluster, which reduces the covalency of the bridge in the Fe_2S_2 sub-cluster. The overall result of this structural difference is a significant reduction in the covalency of the bridging ligands from 61% in Fe_2S_2 to 39% in the Fe_2S_2 unit of the Fe_4S_4 cluster [93,94]. The reduction of covalency of the bridging ligands decreases the superexchange and tends to help delocalization.

Using the experimentally determined value $J = 360\,cm^{-1}$ [120,121] for a reduced Fe_2S_2 cluster as a reference, the J value for the Fe_2S_2 site of Fe_4S_4 model complexes was estimated from these experimentally determined covalency differences to be $147\,cm^{-1}$.

The double exchange parameter B, which reflects the extent of electron delocalization in the Fe_2S_2 units, was determined from geometry optimized DFT calculations of these model complexes. The calculated B was calibrated against the experimentally observed B of $Fe_2\mu$-$(OH)_3L_2$ [121]. Vibronic coupling was estimated from normal coordinate analyses of Fe_2S_2 and Fe_4S_4 data [122]. The values of J, B and $\lambda^2/2k$ estimated from S K-edge experiment and calculations are listed in Table 15.

Using these values, the energies of the spin states are plotted using Eq. (10) (Fig. 30). In the case of Fe_4S_4 the Fe_2S_2 sub-cluster has a delocalized $S = 9/2$ ground state. However the Fe_2S_2 site of a reduced Fe_2S_2 cluster has a localized $S = 1/2$ ground state. Thus, while spin frustration will contribute to the energies of the spin states of Fe_4S_4 cluster, its important to note that the $S = 9/2$ by decreasing delocalized ground state can be reached the covalency of the bridging ligands as a result of the additional bonding interactions within these clusters. This difference in delocalization can make a significant contribution to the electron transfer properties of these centers.

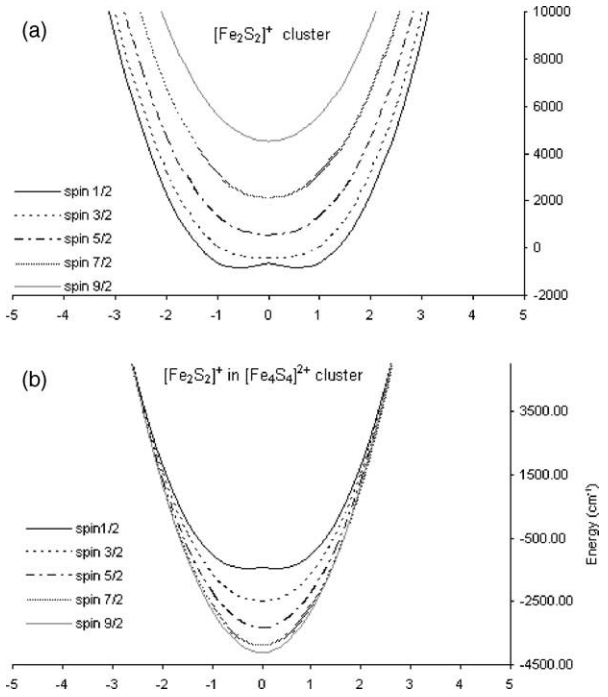

Fig. 30. Potential energy surfaces of the dimer subsite spin states in the mixed-valence (a) binuclear (b) tetranuclear Fe–S cluster in the dimensionless antisymmetric breathing mode x^- (calculated using Eq. (10) with the values given in Table 15).

As mentioned in Section 5.4.1 a similar decrease in covalency has been observed in the $[Fe_2S_2]^+$ subunit of the $[Fe_3S_4]^0$ cluster is much lower than that of the reduced $[Fe_2S_2]$ cluster. The impact of this decrease on the exchange interaction in the cluster and on the potential energy surface of different spin states is currently under investigation.

6. Ni dithiolene complexes

The transition metal bound dithiolene complexes are structurally well-defined compounds with relevance to the Mo-pterin-dithiolene cofactor in mononuclear oxotransferases [123] such as xanthine oxidase, sulfite reductase, and DMSO reductase. Understanding the bonding between the metal and the dithiolene ligand can provide insight into structure/function relationships in these metalloenzymes.

Table 15
Estimated J, B and $\lambda^2/2k$ values for Fe_2S_2 unit in bi-, tetranuclear Fe–S clusters

Core	Fe–S covalency[a] (%)			Estimate of J (cm^{-1})	Estimate of B (cm^{-1})	Estimate of $\lambda^2/2k$ (cm^{-1})
	μ_3	μ_2	Average			
$[Fe_2S_2]^+$		61	61	−360	850	3660
$[Fe_2S_2]^+$ In Fe_4S_4	39		39	−147	1550	3190

[a] Averaged over Fe_2S_2 subsite in these clusters.

These complexes are also of importance in reactions with olefins [124].

The first complete series of non-benzeneoid bis(dithiolene) complexes over three oxidation states, $[Ni(S_2C_2Me_2)_2]^Z$, $Z = 2-$, $1-$ and 0, has been recently isolated and characterized structurally by Holm and co-workers [125]. The bonding in the paramagnetic, monoanionic complex has been defined by EPR [126,127] and ENDOR/ESEEM [128] spectroscopies to be highly covalent with the spin delocalized predominantly over the sulfur atoms. The dianionic complex has been described as a normal Ni^{2+} ion with two ene-1,2-dithiolate ligands [129]. In the literature, there are two ground state bonding descriptions for the neutral complex both assuming a Ni^{2+} oxidation state: (i) diradical with the spin localized on the ligands [130] and (ii) delocalized resonance pair between enedithiolate and dithioketone ligand forms [131]. S K-edge X-ray absorption spectroscopy allows for defining the bonding over the three oxidation states including both diamagnetic complexes.

6.1. Transition dipole integral for dithiolene-S

The transition dipole integrals, which are essential in quantifying the XAS pre-edge intensities, have already been determined for sulfide ($I(S^s) = 6.54$) [85] and thiolate ($I(S^t) = 8.05$) [85]. A new transition dipole integral is needed for the dithiolene-S, due to the different electronic nature of the enedithiolate sulfur. In the free enedithiolate ligand, electron density is delocalized from the S 3p orbital into the π-bond, resulting in an increase of the effective nuclear charge (Z_{eff}) on the sulfur, hence in a more stabilized S 1s orbital. Using the S K-edge spectra of the free S-ligands, including anhydrous Na_2S, NaSEt and $Na_2(S_2C_2H_2)$ (Fig. 31), the energies of the rising edges from the S 1s → 4p transitions were estimated to be 2472.3, 2473.4, and 2474.2 eV, respectively [132]. Assuming a linear relationship [26,30] between the energy positions of the edge jumps and the transition dipole integrals (due to orbital contraction with increasing Z_{eff}), the dithiolene-S transition dipole in the ligand salt was estimated to be 9.15, which needs to be further adjusted in Ni bis(dithiolene) complexes due to the

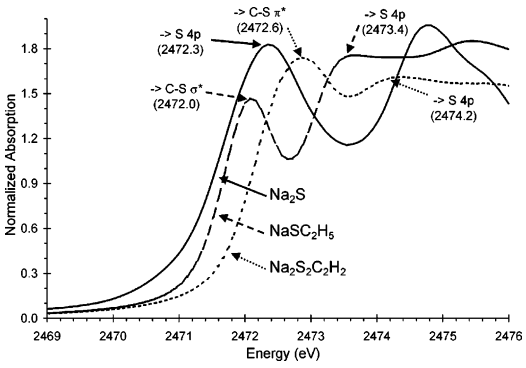

Fig. 31. S K-edge XAS spectra of sulfide (—), thiolate (· · ·) and enedithiolate (- - -) sodium salts (energies in parenthesis in eV).

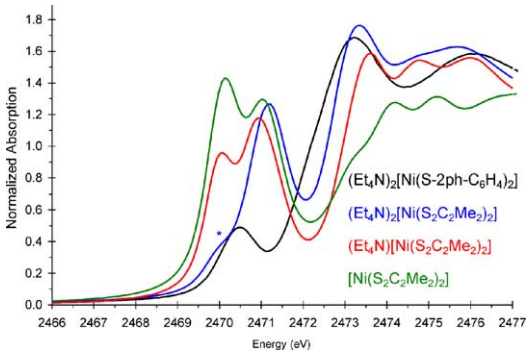

Fig. 32. S K-edge spectra of Ni bis(dithiolenes) complexes $[Ni(S_2C_2Me_2)_2]^Z$, $Z = 2-$ (blue line), $Z = 1-$ (red line), $Z = 0$ (green line) and a Ni tetrathiolate complex (black line).

significant electron donation from the ligand to the metal (see below).

6.2. Bonding in $[Ni(S_2C_2Me_2)_2]^Z$, $Z = 2-$, $1-$ and 0 complexes

The S K-edge spectra of the $[Ni(S_2C_2Me_2)_2]^Z$ series are shown in Fig. 32 [132]. The change in the energy positions of the pre-edge features and rising edge jumps along the series are very different from those of the tetrathiolate complexes [71]. The rising edge positions of the ferrous/ferric tetrathiolates shift up by 0.5 eV, indicating a shift of the S 1s orbital to higher binding energy and hence an increase in Z_{eff} (Section 5.1.2, Fig. 17). Simultaneously, the pre-edge positions shift to lower energy by 1.0 eV in the thiolate complexes, indicating stabilization of the d-manifold. For the Ni bis(dithiolene) complexes, the pre-edge energy positions do not change upon oxidation, while the rising edge positions shift to higher energy by 0.4 eV. The smaller change in the d-manifold of the Ni bis(dithiolene) complexes (0.4 eV) compared to the Fe tetrathiolate complexes (1.5 eV) indicates a significantly smaller change in Z_{eff} of the metal and thus indicating ligand character in the valence orbitals of the bis(dithiolene) complexes. Fig. 32 also includes the S K-edge spectrum of the $(Et_4N)_2[Ni(S\text{-}2Ph\text{-}C_6H_4)_4]$ tetrahedral Ni^{2+} (vide supra Fig. 16) tetrathiolate. The ground state of this complex is a triplet and the pre-edge feature at 2470.5 eV can be attributed to a doubly degenerate S 1s → $\pi^*(t_2)$ transition, which quantifies to be 33% in S 3p character for each of the t_2 holes [132]. In contrast to the bis(dithiolene) complexes (vide infra), the Ni tetrathiolates are characterized by a normal bonding description (Scheme 1A) with predominantly metal-based LUMOs. The shift in the rising edge positions (0.7 eV) of the Ni(II) tetrathiolate and bis(dithiolene) complexes in Fig. 32 correlates well with the difference in the edge jump positions of the thiolate and the enedithiolate sodium salts. Thus, the 0.7 eV shift in the pre-edge energy feature implies no change in the energy of the d-manifold, which is in contrast to what is generally observed in going from a tetrahedral to a square-planar coordination geom-

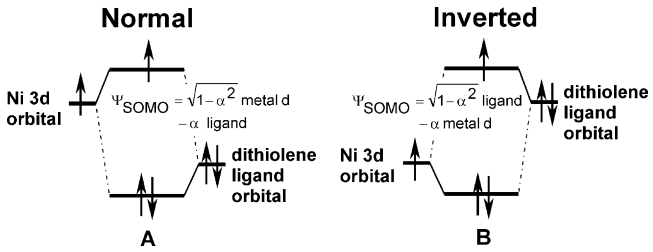

Scheme 1.

etry. The approximately two-fold increase in the pre-edge intensity indicates significantly more covalent bonding in the bis(dithiolene) complex even with the increase in the dithiolene-S transition dipole integral relative to that of the thiolate-S.

The pre-edge energy region of the background-corrected spectra (using the $Na_2(S_2C_2H_2)$ salt spectrum) are shown in Fig. 33. The intense pre-edge features are characteristic of highly covalent, S based metal–ligand bonds. In going from the dianionic form with one pre-edge transition at ~2471 eV to the monoanionic complex, a new pre-edge feature is observed at ~2470 eV with approximately half of the intensity of the 2471.0 peak. This corresponds to the singly occupied orbital probed by EPR spectroscopy. Further oxidation to the neutral complex approximately doubles the intensity of the lower energy pre-edge feature with virtually no change in the energy positions of both features. Since the rising edge positions of the bis(dithiolene) complexes significantly shifts to higher energy by 0.4 eV in the order of $Z = 2-$, 1–, and 0, the transition dipole integral developed for the ligand salt needs to be further increased and thus, the pre-edge transitions quantify to 77% in $Z = 2-$, 59 and 71% in $Z = 1-$, and 67 and 57% in $Z = 0$, for the lower and higher energy features, respectively.

The donor orbitals of the bis(dithiolene) ligands (without the central metal atom) have been evaluated by density functional calculations to account for ligand–ligand repulsion. Fig. 34A shows the two highest occupied in-plane σ and out-of-plane π molecular orbitals. The HOMO(σ_-^-) and the HOMO-1(π_3^-) orbitals have good overlap with the Ni

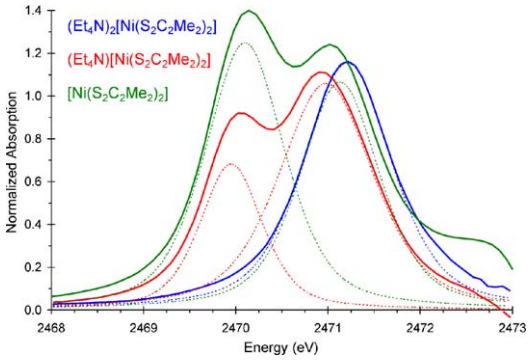

Fig. 33. Representative fits of the pre-edge features of Ni bis (dithiolene) complexes $[Ni(S_2C_2Me_2)_2]^Z$, $Z = 2-$ (blue), $Z = 1-$ (red), $Z = 0$ (green).

$3d_{xy}$ and $3d_{xz}$ orbitals, respectively, allowing for efficient ligand-to-metal electron donation. These two ligand orbitals are dominantly responsible for bonding in Ni bis(dithiolene) complexes, while lower lying orbitals, such as σ_-^+ and π_3^+, can mix with the Ni 4p orbitals; however, they are not probed by S K-edge XAS. Due to the short interligand S . . . S distances, the significant ligand–ligand repulsion between the two enedithiolates results in more destabilized donor ligand orbitals (Fig. 34A) than the empty metal d-orbitals and hence an inverted bonding description (Scheme 1B) with dominant S ligand character in the antibonding valence orbitals.

Fig. 34B shows the LUMO of the dianionic Ni bis(dithiolene) complex, which gives the pre-edge transition at ~2471 eV in Fig. 33. This orbital is an antibonding combination of the Ni $3d_{xy}$ and bis(dithiolene) ligand σ^- orbital. It has primarily ligand character with 53% S 3p contribution as calculated using the BP86 functional and a theoretically converged basis set, which is too ionic compared to the experimental value of 77%. The van Leeuwen–Baerends functional (LB94) [133,134] is found to give the most reasonable description of the ground state with 63% S character. Contrary to the literature, the dianionic complex should not be described as a normal Ni(II) complex, since it has much more electron density donated from the ligand to the Ni in the bis(dithiolene) complexes than for example in the tetrathiolates due to the strong intra- and inter-ligand–ligand repulsion, which increases the energies of these orbitals and leads to the inverted bonding scheme in Scheme 1B.

Upon oxidation of the dianionic Ni bis(dithiolene) complex, an electron hole is created in the highest lying, occupied π-type orbital, shown in Fig. 34B, which is formed by an antibonding combination of Ni $3d_{xz}$ and dithiolene π_3^- orbitals (using a butadiene-like MO description). The GGA density functional calculations, such as BP86, give a ground state sulfur covalency of 60% in the π-type orbital in good agreement with covalencies from S K-edge (59 ± 3%) and EPR (55 ± 5%) spectroscopies. Thus, EPR, ENDOR, ESEEM and XAS results converge to a common, highly covalent ground state bonding description for the monoanionic Ni bis(dithiolene) complex with the unique ability of the XAS to also probe doubly unoccupied (diamagnetic) orbitals.

In the neutral complex, both σ- and π-type orbitals are doubly unoccupied and give rise to the two intense pre-edge features in Fig. 33. The qualitative description of these two orbitals is very similar to those of the anionic complexes. The hybrid DFT calculations with a mixing of 10% Hartree–Fock exchange gives a good fit (62 and 57%) to the experimental orbital covalencies (67 and 57% S 3p character in out-plane LUMO and in-plane LUMO + 1, Fig. 34B), which indicate predominantly S-based electron holes. The reasonably small HOMO/LUMO gap (1.1 eV from calculations) of the neutral complex and the symmetries of the two frontier orbitals (both are based on combinations of the π_3 ligand orbitals) can allow for some limited mixing, and thus spin polarization of the ground state wave function. This can be illustrated by Fig. 35, which shows various degrees of spin localiza-

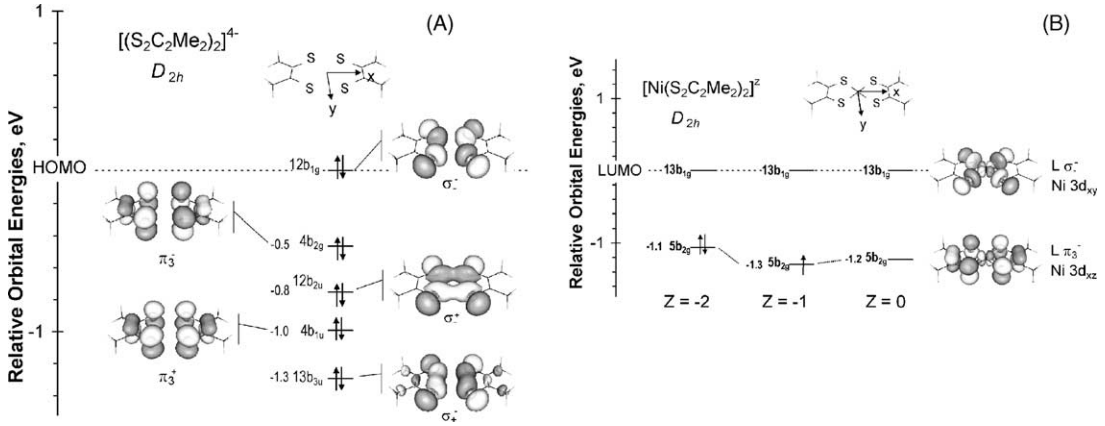

Fig. 34. Orbital energy levels for the frontier orbitals of the bis(dithiolene) ligand system (A) and for the Ni bis(dithiolene) complexes (B).

tions (0.2 and 0.9 spin on each ligands with opposite sign in Fig. 35A and B, respectively) depending on the amount of Hartree–Fock exchange in the hybrid density functional calculation. In agreement with others [135], these spectroscopically calibrated DFT calculations show only limited spin localization (at most 0.4 electron on each ligand) in the neutral complex reflecting the highly covalent, delocalized ground state description experimentally determined from ligand K-edge XAS.

6.3. Reactivity of the $[Ni(S_2C_2Me_2)_2]$ complex with olefins

Wang and Stiefel recently [124] and Schrauzer and Mayweg earlier [136] have shown the non-classical reactivity of the neutral Ni bis(dithiolene) complexes, which can now be explained by the inverted ground state bonding (Scheme 1B). The neutral complex reacts with olefins in electrophilic addition to form an adduct, where the C atoms of the olefin are bound to the S atoms of the bis(dithiolene) complex, instead of forming a classical π-complex with the central Ni atom. Due to the large electron donation from the ligand to the metal, the S atoms become more electrophilic than the Ni, favoring the reaction of the S atoms with olefins. The ligand-based acceptor LUMOs, which are probed by S K-edge XAS, are set up for the interaction with the donor olefin HOMO (Scheme 2).

In Scheme 2, two different olefin coordinations are shown to give interligand (Scheme 2A) and intraligand (Scheme 2B) olefin adducts. In the former case, the LUMO of the bis(dithiolene) complex does not give a net bonding interaction with the HOMO of the olefin. A recent DFT study [137] has shown that this orbital forbiddeness can be overcome by an out-of-plane distortion of the bis(dithiolene) complex into a flattened D_{2d} structure, where the olefin HOMO can overlap with the opposite sides of the S centered lobes of the bis(dithiolene) LUMO. This addition gives a *trans* product, which can isomerize to the *cis* interligand adduct. The D_{2d} distortion and olefin coordination has been calculated as the rate-limiting step with 113 kJ mol^{-1} activation barrier, which is approximately 20 kJ mol^{-1} higher than the experimental value. Alternatively, for the intra-ligand interaction in Scheme 2B, the LUMO of the neutral Ni bis(dithiolene) complex can interact with the HOMO of the olefin to give a net bonding interaction leading to an intraligand adduct with a lower activation barrier, since the bis(dithiolene) complex does not need to be significantly distorted. Spectroscopically calibrated hybrid density functional studies indicate that rate-limiting activation barriers of inter- and intraligand olefin coordinations are comparable with a slight preference of 12 kJ mol^{-1} for the latter in agreement with the FMO analysis above. In addition, the singlet/triplet gap for the bis(dithiolene) complex (about 45 kJ mol^{-1}) is comparable to the activation barrier of the olefin coordination to the singlet complex and the singly unoccupied orbitals can also provide bonding interactions with the olefin HOMO, which could allow for additional reaction pathways on the triplet potential energy surface.

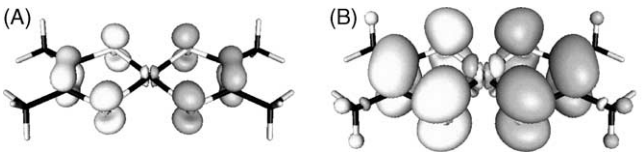

Fig. 35. Spin density contour plots of the spin polarized wave function for $[Ni(S_2C_2Me_2)_2]$ at (A) B(22HF)P86/BS5 and (B) B(50HF)P86/BS5 levels of theory.

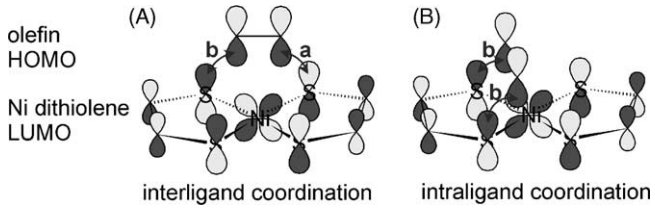

Scheme 2.

7. Concluding comments

From this review it should be clear that ligand K-edge XAS provides a powerful experimental probe of the covalency of the ligand–metal bond. Combined with metal L-edge spectroscopy, which probes the metal d-character in a wavefunction, and metal K-edge spectroscopy, which probes the metal p character, one can experimentally define many of the key features of a ground state wavefunction. This is extremely important in the context of modern electronic structure theory as it provides an experimental approach to evaluate the applicability of different types of DFT calculations. As illustrated in this review, understanding the covalency of ligand–metal bonds is also critical in understanding reactivity. We have illustrated this with electron transfer pathways, H-bond effects on reduction potentials, and activation of a metal complex for reactivity with olefins. Many applications have thus far been in the field of bio-inorganic chemistry. These continue to evolve in a number of directions including the definition of electronic relaxation in iron–sulfur redox processes, the role of trans axial thiolate bonding in the reactivity of non-heme and heme active sites and the contribution of dithiolene bonding to the activation of oxo-molybdenum transferases. However this ligand K-edge methodology is general and should also have impact in many areas of inorganic chemistry including organometallics and catalysis.

Acknowledgements

This work was supported by grants NIH RR-01209 (K.O.H.), and NSF CHE-9980549 (E.I.S.). SSRL operations are funded by the Department of Energy, Office of Basic Energy Sciences. The SSRL Structural Molecular Biology program is supported by the National Institutes of Health, National Center for Research Resources, Biomedical Technology Program and by the Department of Energy, Office of Biological and Environmental Research. We gratefully acknowledge the contributions of our co-workers and collaborators, who are cited in the referenced publications.

References

[1] E.I. Solomon, in: N. Sutin (Ed.), Comments on Inorganic Chemistry, vol. III, Number 5, Gordon and Breach, New York, 1984, p. 225.
[2] B.M. McGarvey, in: Trans. Met. Chem., vol. 3, R.L. Carlin (Ed.), Marcel-Dekker, 1967. Chap. Electron Spin Resonance of Transition-Metal Complexes, p. 89.
[3] K.W. Penfield, A.A. Gewirth, E.I. Solomon, J. Am. Chem. Soc. 107 (1985) 4519.
[4] B.A. Goodman, Radio. Chem. 13 (1975) 135.
[5] J.R. Pirbrow, Transition Ion Electron Paramagnetic Resonance, Oxford University Press, London, 1990.
[6] F. Tuczek, E.I. Solomon, Coord. Chem. Rev. 219 (2001) 1075.
[7] S.V. Didziulis, S.L. Cohen, A.A. Gewirth, E.I. Solomon, J. Am. Chem. Soc. 110 (1988) 250.
[8] (a) B. Hedman, K.O. Hodgson, E.I. Solomon, J. Am. Chem. Soc. 112 (1990) 1643;
(b) T. Glaser, B. Hedman, K.O. Hodgson, E.I. Solomon, Acc. Chem. Res. 33 (2000) 859.
[9] J.E. Hahn, R.A. Scott, K.O. Hodgson, S. Doniach, S.R. Desjardins, E.I. Solomon, Chem. Phys. Lett. 88 (1982) 595.
[10] (a) T.E. Westre, P. Kennepohl, J.G. DeWitt, B. Hedman, K.O. Hodgson, E.I. Solomon, J. Am. Chem. Soc. 119 (1997) 6297;
(b) C. Randall, L. Shu, Y. Chiou, K.S. Hagen, M. Ito, N. Kitajima, R.J. Lachicotte, Y. Zang, L. Que Jr., Inorg. Chem. 34 (1995) 1036.
[11] H. Wang, G. Peng, L.M. Miller, E.M. Scheuring, S.J. George, M.R. Chance, S.P. Cramer, J. Am. Chem. Soc. 119 (1997) 4921.
[12] S.J. George, M.D. Lowery, E.I. Solomon, S.P. Cramer, J. Am. Chem. Soc 115 (1993) 2968.
[13] M.D. Lowery, J.A. Guckert, M.S. Gebhard, E.I. Solomon, J. Am. Chem. Soc. 115 (1993) 3012.
[14] F.W. Lytle, R.B. Greegor, D.R. Sandstrom, E.C. Marques, J. Wong, C.L. Spiro, G.P. Huffman, F.E. Huggins, Nucl. Instrum. Methods 226 (1984) 542.
[15] E.A. Stern, S.M. Heald, Rev. Sci. Instrum. 50 (1979) 1579.
[16] The EXAFS Company, HC 74 Box 236, Eagle Valley Road, Pioche, NV 89043.
[17] J. Stöhr, Principles, Techniques, and Instrumentation of NEXAFS in NEXAFS Spectroscopy, Springer-Verlag, Berlin, 1992, p. 133 (Chapter 5.3).
[18] J. Stöhr, Principles, Techniques, and Instrumentation of NEXAFS in NEXAFS Spectroscopy, Springer-Verlag, Berlin, 1992, p. 118 (Chapter 5.2).
[19] G.N. George, EDG_FIT, Stanford Synchrotron Radiation Laboratory, Stanford Linear Accelerator Center, Stanford University, Stanford CA, USA.
[20] B.S. Garbow, K.E. Hillstrom, J.J. More, MINPAK Fitting Library Argonne National Laboratory, Argonne, IL, USA.
[21] B.K. Agarwal, X-ray Spectroscopy, Springer-Verlag, Berlin, 1979.
[22] T.A. Tyson, A.L. Roe, P. Frank, K.O. Hodgson, B. Hedman, Phys. Rev. B 39A (1989) 6305.
[23] F.W. Lytle, Applications of Synchrotron Radiation, H. Winick, D. Xian, M.H. Ye, T. Huang (Eds.), Gordon & Breach, New York, 1989.
[24] B. Hedman, K.O. Hodgson, E.I. Solomon, J. Am. Chem. Soc. 112 (1990) 1643.
[25] J.B. Avery, The Quantum Theory of Atoms, Molecules and Photons, McGraw-Hill, London, 1972.
[26] F. Neese, B. Hedman, K.O. Hodgson, E.I. Solomon, Inorg. Chem. 38 (1999) 4854.
[27] S.E. Shadle, B. Hedman, K.O. Hodgson, E.I. Solomon, Inorg. Chem. 33 (1994) 4235.
[28] M.A. Hitchman, J. Chem. Soc., Chem. Comm. (1979) 973.
[29] J.J. Ferguson, Chem. Phys. 40 (1964) 3406.
[30] S.E. Shadle, B. Hedman, K.O. Hodgson, E.I. Solomon, J. Am. Chem. Soc. 117 (1995) 2259.
[31] E.P. Wigner, Group Theory and its Application to the Quantum Mechanics of Atomic Spectra, Translated from the German by J.J. Griffin., 1959, 383 pp.
[32] W. Koch, M.C. Holthausen, A Chemist's Guide to Density Functional Theory, Wiley-VCH, Weinheim, 2000.
[33] E.I. Solomon, R.K. Szilagyi, S. DeBeer George, L. Basumallick, Chem. Rev. 104 (2004) 419.
[34] R.S. Mulliken, J. Chem. Phys. 23 (1955) 1833.
[35] R.F.W. Bader, Atoms in Molecules: A Quantum Theory Oxford University Press, Oxford, 1990.
[36] J.P. Foster, F. Weinhold, J. Am. Chem. Soc. 102 (1980) 7211.
[37] F. Maseras, K. Morokuma, Chem. Phys. Lett. 195 (1992) 500.
[38] G. te Velde, Numerical integration and other methodological aspects of bandstructure calculations, Thesis, Universiteit Amsterdam, Vrije, 1990.
[39] F.L. Hirshfeld, Theo. Chim. Acta 44 (1977) 129.

[40] R.H. Holm, P. Kennepohl, E.I. Solomon, Chem. Rev. 96 (1996) 2239.
[41] J.M. Guss, H.C. Freeman, J. Mol. Biol. 169 (1983) 521.
[42] E.T. Adman, J.W. Godden, S. Turley, J. Biol. Chem. 270 (1995) 27458.
[43] P.J. Hart, A.M. Nesissian, R.G. Herrmann, R.M. Nalbandyan, J.S. Valentine, D. Eisenberg, Prot. Sci. 5 (1996) 2175.
[44] V. Ducros, A.M. Brzozowski, K.S. Wilson, S.H. Brown, P. Ostergaard, P. Schneider, D.S. Yaver, A.H. Pedersen, G.J. Davies, Nat. Struct. Biol. 5 (1998) 310.
[45] E.I. Solomon, K.W. Penfield, A.A. Gewirth, M.D. Lowery, S.E. Shadle, J.A. Guckert, L.B. LaCroix, Inorg. Chim. Acta 243 (1996) 67.
[46] K.W. Penfield, R.R. Gay, R.S. Himmelwright, N.C. Eickman, H.C. Freeman, E.I. Solomon, J. Am. Chem. Soc. 103 (1981) 4382.
[47] H. Beinert, Eur. J. Biochem. 245 (1997) 521.
[48] T. Haltia, K. Brown, M. Tegoni, C. Cambillau, M. Saraste, K. Mattila, K. Djinovic-Carugo, Biochem. J. 369 (2003) 77.
[49] S. Ferguson-Miller, G.T. Babcock, Heme/Copper Terminal Oxidases 96 (1996) 2889.
[50] B.E. Ramirez, B.G. Malmström, J.R. Winkler, H.B. Gray, Proc. Natl. Acad. Sci. USA 92 (1995) 11949.
[51] H. Robinson, M.C. Ang, Y.-G. Gao, M.T. Hay, Y. Lu, A.H.-J. Wang, Biochemistry 38 (1999) 5676.
[52] R.P. Houser, V.G. Young Jr., W.B. Tolman, J. Am. Chem. Soc. 118 (1996) 2101.
[53] S.E. Shadle, J.E. Penner-Hahn, H.J. Schugar, B. Hedman, K.O. Hodgson, E.I. Solomon, J. Am. Chem. Soc. 115 (1993) 767.
[54] J.L. Hughley, T.G. Fawcett, S.M. Rudich, R.A. Lalancette, J.A. Potenza, H.J. Schugar, J. Am. Chem. Soc. 101 (1979) 2617.
[55] A.A. Gewirth, S.L. Cohen, H.J. Schugar, E.I. Solomon, Inorg. Chem. 261 (1987) 1133.
[56] R.K. Szilagyi, M. Metz, E.I. Solomon, J. Chem. Phys. A 106 (2002) 2994.
[57] A.E. Reed, L.A. Curtiss, F. Weinhold, Chem. Rev. 88 (1988) 899.
[58] J.E. Carpenter, F.J. Weinhold, Mol. Struct. (THEOCHEM) 169 (1988) 41.
[59] A.D. Becke, Phys. Rev. A Gen. Phys. 38 (1988) 3098.
[60] A.D. Becke, J. Chem. Phys. 98 (1993) 5648.
[61] C. Lee, W. Yang, R.G. Parr, Phys. Rev. B Condens. Matter 37 (1988) 785.
[62] K. Brown, M. Tegoni, M. Prudencio, A.S. Pereira, S. Besson, J.J. Moura, I. Moura, C. Cambillau, Nat. Struct. Biol. 7 (2000) 191.
[63] S. DeBeer George, L. Basumallick, R.K. Szilagyi, D.W. Randall, M.G. Hill, A.M. Nersissian, J.S. Valentine, B. Hedman, K.O. Hodgson and E.I. Solomon, J. Am. Chem. Soc. 125 (2003) 11314.
[64] S. DeBeer George, M. Metz, R.K. Szilagyi, H. Wang, S.P. Cramer, Y. Lu, W.B. Tolman, B. Hedman, K.O. Hodgson, E.I. Solomon, J. Am. Chem. Soc. 123 (2001) 5757.
[65] D.R. Gamelin, D.W. Randall, M.T. Hay, R.P. Houser, T.C. Mulder, G.W. Canters, S. de Vries, W.B. Tolman, Y. Lu, E.I. Solomon, J. Am. Chem. Soc. 120 (1998) 5246.
[66] R.K. Szilagyi, E.I. Solomon, Curr. Opin. Chem. Biol. 6 (2002) 250.
[67] M.D. Newton, Chem. Rev. 91 (1991) 767.
[68] J.M. Guss, E.A. Merritt, R.P. Phizackerley, H.C. Freeman, J. Mol. Biol. 259 (1996) 686.
[69] P. Siders, R.A. Marcus, J. Am. Chem. Soc. 103 (1981) 741.
[70] R.A. Marcus, N. Sutin, Biochim. Biophys. Acta 811 (1985) 265.
[71] K. Rose Williams, B. Hedman, K.O. Hodgson, E.I. Solomon, Inorg. Chim. Acta 263 (1997) 315.
[72] K. Rose Williams, S.E. Shadle, M.K. Eidsness, D.M. Kurtz Jr., R.A. Scott, B. Hedman, K.O. Hodgson, E.I. Solomon, J. Am. Chem. Soc. 120 (1998) 10743.
[73] M.S. Gebhard, J.C. Deaton, S.A. Koch, M. Millar, E.I. Solomon, J. Am. Chem. Soc. 112 (1990) 2217.
[74] Crystal structures obtained from Cambridge Crystallographic Database Ver. 1.5.; F.H. Allen, O. Kennard, Chemical Design Automation News 8 (1993) 1 and 31.
[75] I. Bertini, A. Sigel, H. Sigel (Eds.), Handbook of Metalloproteins, Marcel Dekker, New York, 2001.
[76] W.R. Dunham, A.J. Bearden, I.T. Salmeen, G. Palmer, R.H. Sands, W.H. Orme-Johnson, H. Beinert, Biochim. Biophys. Acta 253 (1971) 134.
[77] P.J. Hay, J.C. Thibeault, R.J. Hoffman, J. Am. Chem. Soc. 97 (1975) 4884.
[78] L. Peterson, R. Cammack, K.K. Rao, Biochim. Biophys. Acta 622 (1980) 18.
[79] P. Bertrand, J.-P. Gadaya, Biochim. Biophys. Acta 680 (1982) 331.
[80] L. Noodleman, E.J. Baereands, J. Am. Chem. Soc. 106 (1984) 2316.
[81] G. Blondin, J.-J. Girerd, Chem. Rev. 90 (1990) 1359.
[82] M.K. Johnson, Curr. Opin. Chem. Biol. 2 (1998) 173.
[83] B.R. Crouse, J. Meyer, M.K. Johnson, J. Am. Chem. Soc. 117 (1995) 9612.
[84] J. Fujinaga, J. Gaillard, J. Meyer, Biochem. Biophys. Res. Commun. 194 (1993) 104.
[85] K. Rose, S.E. Shadle, T. Glaser, S. de Vries, A. Cherepanov, G.W. Canters, B. Hedman, K.O. Hodgson, E.I. Solomon, J. Am. Chem. Soc. 121 (1999) 2353.
[86] K.D. Butcher, M.S. Gebhard, E.I. Solomon, Inorg. Chem. 29 (1990) 2067.
[87] J. Li, M.R. Nelson, C.Y. Peng, D. Bashford, L. Noodleman, J. Phys. Chem. A 102 (1998) 6311.
[88] E. Anxolabéhère-Mallart, T. Glaser, P. Frank, A. Aliverti, G. Zanetti, B. Hedman, K.O. Hodgson, E.I. Solomon, J. Am. Chem. Soc. 123 (2001) 5444.
[89] P.K. Mascharak, G.C. Papaefthymiou, R.B. Frankel, R.H. Holm, J. Am. Chem. Soc. 103 (1981) 6110.
[90] J.J. Mayerle, S.E. Denmark, B.V. DePamphilis, J.A. Ibers, R.H. Holm, J. Am. Chem. Soc. 97 (1975) 1032.
[91] K.S. Hagen, A.D. Watson, R.H. Holm, J. Am. Chem. Soc. 105 (1983) 3905.
[92] H.A. Heering, Y.B.M. Bulsink, W.R. Hagen, T.E. Meyer, Biochemistry 34 (1995) 14675.
[93] T. Glaser, K. Rose, S.E. Shadle, B. Hedman, K.O. Hodgson, E.I. Solomon, J. Am. Chem. Soc. 123 (2001) 442.
[94] A. Dey, B. Hedman, K.O. Hodgson, E.I. Solomon, J. Am. Chem. Soc. (accepted for publication).
[95] K.S. Hagen, A.D. Watson, R.H. Holm, J. Am. Chem. Soc. 105 (1983) 3905.
[96] B.A. Averill, T. Herskovitz, R.H. Holm, J.A. Ibers, J. Am. Chem. Soc. 95 (1973) 3523.
[97] M.K. Johnson, R.E. Duderstadt, E.C. Duin, Adv. Inorg. Chem. 47 (1999) 1.
[98] H. Beinert, A.J. Thomson, Arch. Biochem. Biophys. 333 (1983) 222.
[99] V. Papaefthymiou, J.-J. Girerd, I. Moura, J.J.G. Moura, E. Münck, J. Am. Chem. Soc. 109 (1987) 4703.
[100] S.A. Borshch, E.L. Bominaar, G. Blondin, J.-J. Girerd, J. Am. Chem. Soc. 115 (1993) 5155.
[101] L. Noodleman, D.A. Case, A. Aizmanf, J. Am. Chem. Soc. 110 (1988) 1001.
[102] J. Zhou, Z. Hu, E. Münck, R.H. Holm, J. Am. Chem. Soc. 118 (1996) 1966.
[103] A. Dey, B. Hedman, K.O. Hodgson, E.I. Solomon, unpublished results.
[104] T.G. Spiro (Ed.), Iron Sulfur Proteins, Wiley, New York, 1982.
[105] D.W. Low, M.G. Hill, J. Am. Chem. Soc. 122 (2000) 11039.
[106] E. Babini, M. Borsari, F. Capozzi, L.D. Eltis, C. Luchinat, J. Biol. Inorg. Chem. 4 (1999) 692.
[107] N. Ueyama, Y. Yamada, T. Okamura, S. Kimura, A. Nakamura, Inorg. Chem. 35 (1996) 6473.
[108] E. Denke, T. Merbitz-Zahradnik, O.M. Hatzfeld, C.H. Snyder, T.A. Link, B.L. Trumpower, J. Biol. Chem. 273 (1998) 9085.

[109] K. Bose, J. Huang, B.S. Haggerty, A.L. Rheingold, R.J. Salm, M.A. Walters, Inorg. Chem. 36 (1997) 4596.
[110] J. Li, M.R. Nelson, C.Y. Peng, D. Bashford, L. Noodleman, J. Phys. Chem. A 102 (1998) 6311.
[111] G.M. Jensen, A. Warshel, P.J. Stephens, Biochemistry 33 (1996) 10911.
[112] E. Parisini, F. Capozzi, P. Lubini, V. Lamzin, C. Luchinat, G.M. Sheldrick, Acta Crystallogr. D55 (1999) 1773.
[113] Z. Dauter, K.S. Wilson, L.C. Sieker, J. Meyer, J.-M. Moulis, Biochemistry 36 (1997) 16065.
[114] T. Glaser, I. Bertini, J.J.G. Moura, B. Hedman, K.O. Hodgson, E.I. Solomon, J. Am. Chem. Soc. 123 (2001) 4859.
[115] B.J. Goodfellow, A.L.M. Rodrigues, I. Moura, V. Wray, J.J.G. Moura, J. Biol. Inorg. Chem. 4 (1999) 421.
[116] E.L. Bominaar, Z.G. Hu, E. Münck, J.-J. Girerd, S.A. Borshch, J. Am. Chem. Soc. 117 (1995) 6976.
[117] C. Zener, Phys. Rev. 82 (1951) 403.
[118] A. Kramer, Physica 1 (1934) 191.
[119] J.-J. Girerd, J. Chem. Phys. 79 (1983) 1766.
[120] D.R. Gamelin, E.L. Bominaar, C. Mathonière, M.L. Kirk, K. Wieghardt, J.-J. Girerd, E.I. Solomon, Inorg. Chem. 35 (1996) 4323.
[121] D.R. Gamelin, E.L. Bominaar, M.L. Kirk, K. Wieghardt, E.I. Solomon, J. Am. Chem. Soc. 118 (1996) 8085.
[122] R.S. Czernuszewicz, K.A. Macor, M.K. Johnson, A. Gewirth, T.G. Spiro, J. Am. Chem. Soc. 109 (1987) 7178.
[123] R. Hille, Chem. Rev. 96 (1996) 2757.
[124] K. Wang, E.I. Stiefel, Science 291 (2001) 106.
[125] B.S. Lim, V. Fomitchev, R.H. Holm, Inorg. Chem. 40 (2001) 4357.
[126] A.H. Maki, N. Edelstein, A. Davison, R.H. Holm, J. Am. Chem. Soc. 86 (1964) 4580.
[127] R.D. Schmitt, A.H. Maki, J. Am. Chem. Soc. 90 (1968) 2288.
[128] J.E. Huyett, S.B. Choudhury, D.M. Eichhorn, P.A. Bryngelson, M.J. Maroney, B.M. Hoffman, Inorg. Chem. 37 (1998) 1361.
[129] R.H. Holm, M.J. O'Connor, Prog. Inorg. Chem. 14 (1971) 241.
[130] E.I. Stiefel, J.H. Waters, E. Billig, H.B. Gray, J. Am. Chem. Soc. 87 (1965) 3016.
[131] A.L. Balch, R.H. Holm, J. Am. Chem. Soc. 88 (1966) 5201.
[132] R.K. Szilagyi, B.S. Lim, T. Glaser, R.H. Holm, B. Hedman, K.O. Hodgson, E.I. Solomon, J. Am. Chem. Soc. 125 (2003) 9158.
[133] R. van Leeuwen, E.J. Baerends, Phys. Rev. A 49 (1994) 2421.
[134] M. Grüning, O.V. Gritsenko, S.J.A. van Gisbergen, E.J. Baerends, J. Chem. Phys. 114 (2001) 652.
[135] V. Bachler, G. Olbrich, F. Neese, K. Wieghardt, Inorg. Chem. 41 (2002) 4179.
[136] G.N. Schrauzer, V.P. Mayweg, J. Am. Chem. Soc. 87 (1965) 1483.
[137] Y. Fan, M.B. Hall, J. Am. Chem. Soc. 124 (2002) 12076.
[138] I. Bertini, S. Ciurli, A. Dikiy, R. Gasanov, C. Luchinat, G. Martini, N.J. Safarov, J. Am. Chem. Soc. 121 (1999) 2037.
[139] M.M. Werst, C.E. Davoust, B. Hoffman, J. Am. Chem. Soc. 113 (1991) 1533.
[140] F. Neese, R. Kappl, W.G. Zumft, J. Hüttermann, P.M.H. Kroneck, J. Biol. Inorg. Chem. 3 (1998) 53.
[141] R.J. Gurbiel, Y.C. Fann, K.K. Surerus, M.M. Werst, S.M. Musser, P.E. Doan, S.I. Chan, J.A. Fee, B.M. Hoffman, J. Am. Chem. Soc. 115 (1993) 10888.
[142] R.P. Houser, J.A. Halfen, V.G. Young, N.J. Blackburn, W.B. Tolman, J. Am. Chem. Soc. 117 (1995) 10745.